学位申請論文

澁谷拓郎

Multi-trace receiver function inversion of nearby deep earthquake waveforms to estimate S wave velocity structure of the crust and uppermost mantle

Takuo Shibutani
Research Center for Earthquake Prediction
Disaster Prevention Research Institute
Kyoto University
Uji 611, JAPAN
e-mail: shibutan@epdpri1.dpri.kyoto-u.ac.jp

Submitted to GJI on 21 Oct. 1991
Revised on 11 Mar. 1993

Abbreviated title: Multi-trace receiver function inversion.

SUMMARY

To closely examine velocity structure of the upper and lower crust and the uppermost mantle, we inverted radial receiver functions derived from P waveforms of deep earthquakes recorded with STS very broadband seismometers. A site in western Honshu, Japan is studied, that is TTT (Tottori).

We used regional receiver functions which were derived from nearby deep events. The main advantage of using deep events is that the P wave part of their waveform contains larger P-to-S converted waves than teleseismic receiver functions because of the difference of incident angle. Since the P wave part is contaminated by background noises and signal generating noises such as scattered waves due to small scale heterogeneities, the signal-to-noise ratio of the P-to-S converted waves is a most important decisive factor whether a receiver function inversion is successfully done or not.

However, deep events often have various incident angles different by more than several degrees. So we cannot stack the regional receiver functions as previous studies did for teleseismic receiver functions. In order to settle this problem, we developed a new method called 'multi-trace receiver function inversion' in which several receiver functions are inverted simultaneously for one velocity model with their different incident angles. It can also depress effects of the noises on the final models because they are constrained by common phases of all receiver functions.

We modeled the earth's interior down to 60 km as 30 horizontally stratified layers with thicknesses of 2 km and obtained S velocity in each layer. We checked effects of initial models on the resulting final models. The result shows that our inversion can determine an appropriate velocity model on the whole if only an initial model with a proper velocity structure in average is given.

TTT is located in an active fault zone in the Inner zone of Southwest Japan and in an alluvium plain along the coast of the Japan Sea. Two S wave velocity models are obtained along backazimuths of S50°E and S30°E. The two final models are in

good agreement with each other on the whole, especially in the points that the first layer has a low velocity, that the upper part of the lower crust has a structure of alternate high and low velocity and that there is a high velocity layer at the top of the Moho discontinuity.

Key words: receiver function, multi-trace inversion, *S* wave velocity model, crustal structure, uppermost mantle structure.

1 INTRODUCTION

It is very important to obtain detailed velocity structure models of the earth's interior because such models can be useful to investigate the physical properties of the earth's interior. Travel time inversion can show us three-dimensional velocity structure models. However regions modeled by the method are limited because it needs a large dataset. Waveform inversion of long period body waves, surface waves and free oscillations can offer global three-dimensional velocity structure models. Receiver function inversion is a kind of waveform inversion and uses short period body waves, therefore it has a potential to give finer model structure than the other inversion methods. Furthermore, it can basically accomplished with data from one station because waveforms include much more information than travel time data. Receiver function inversion can obtain fine velocity models of the crust and uppermost mantle and answer an question whether the crust-mantle boundary is first order discontinuity or transitional boundary. It is interesting to investigate the regional differences of them and interpret them in relation to tectonics of the region.

Owens, Zandt and Taylor (1984) developed receiver function inversion and obtained a detailed velocity structure model beneath the Cumberland Plateau, Tennessee. Their results indicate that the crust-mantle boundary beneath there is a thick transition zone between the depth of 40 and 55 km and that the midcrustal structure changes significantly in different azimuths. Owens (1987) examined the crustal structure beneath the Adirondack Highlands of upstate New York using the same method and obtained a model with a high velocity zone between 18 and 26 km depth overlying a lower crust of low average velocity. He argued that the high velocity zone correlated in depth with a highly reflective zone in COCORP profiles in the same area.

Ammon (1991) showed a method to estimate the absolute amplitude of the receiver function which provided an additional constraint on the near-surface velocity structure. He also pointed out that the more closer events generated large P-to-

S phases that might rise above a roughly constant scattered wave field, but the converted phases generated by the more distant events might not rise above the background scattering.

In this study we use receiver functions derived from P waveforms of nearby deep earthquakes that are called regional receiver functions. The benefit of using the regional receiver functions is that the P-to-S converted waves have larger amplitude than those in teleseismic receiver functions because the efficiency of P-to-S conversion is better in the case of nearby deep events than teleseismic events. This feature is illustrated in Fig. 1. The absolute amplitude of the P-to-S converted waves, especially Ps, is larger than in the case of the P wave incident angle of 40° that is typical for regional receiver functions than in the case of 25° for teleseismic receiver functions. The signal-to-noise ratio of P-to-S converted phases is very important to obtain a reliable result. And we develop a new method called 'multi-trace receiver function inversion' in which several receiver functions are inverted simultaneously for one velocity model. The main advantage of our method is that it can treat several receiver functions obtained from P waves with different p parameters. It can also depress noise effects on the resulting model because the model is constrained by the common phases of all the receiver functions.

Our study site is TTT in western Honshu, Japan. It is located in an active fault zone in the Inner zone of Southwest Japan. The previous refraction studies in western Honshu, for example, Hashizume et al. (1966), Sasaki et al. (1970) and Yoshii et al. (1974), proposed several velocity structure models for this site. Most of the models are four-layered with the slightly dipping Moho discontinuity towards the east.

2 METHOD

2.1 Receiver Function

The three components of the response at a station due to a P plane wave impinging under a stack of horizontal layers can be theoretically represented by

$$\begin{aligned} D_V(t) &= I(t) * S(t) * E_V(t) \\ D_R(t) &= I(t) * S(t) * E_R(t) \\ D_T(t) &= I(t) * S(t) * E_T(t) \end{aligned} \tag{1}$$

where subscripts V, R and T represent vertical, radial and tangential components, respectively. $I(t)$ is the impulse response of the recording instrument, $S(t)$ is the effective seismic source function of the impinging wave, and $E(t)$ is the impulse response of the earth structure. $S(t)$ may be quite complicated and related to dislocation time history and source area reverberations (Langston 1979). Asterisks represent the convolution operator.

We wish to remove the factor, $I(t) * S(t)$ in the eq.(1) from our observed seismograms to isolate $E_R(t)$ and $E_T(t)$. This can be accomplished by deconvolving $D_V(t)$ from $D_R(t)$ and $D_T(t)$, respectively. To perform this deconvolution stably we divide the Fourier transform of the horizontal components by that of the vertical component after introducing a minimum allowable amplitude level for the amplitude spectrum of the vertical component. The receiver functions are expressed, in the frequency domain,

$$\begin{aligned} R_R(\omega) &= \frac{D_R(\omega)\,\overline{D_V}(\omega)}{\varphi(\omega)}\,G(\omega) \\ R_T(\omega) &= \frac{D_T(\omega)\,\overline{D_V}(\omega)}{\varphi(\omega)}\,G(\omega) \end{aligned} \tag{2}$$

where

$$\varphi(\omega) = max\{D_V(\omega)\,\overline{D_V}(\omega),\ cmax[D_V(\omega)\,\overline{D_V}(\omega)]\} \tag{3}$$

and

$$G(\omega) = e^{-\omega^2/4a^2} \tag{4}$$

In these expressions, c controls the minimum allowable spectral amplitude of the vertical component; α controls the width of a Gaussian function to exclude high frequency noise; and the bar over D_V indicates its complex conjugate. The receiver functions, $R_R(t)$ and $R_T(t)$, are obtained by transforming $R_R(\omega)$ and $R_T(\omega)$ back into the time domain, respectively. Langston (1979) and Owens et al. (1984) assumed that

$$E_V(t) \approx \delta(t)$$

in the case of steeply incident P waves, where $\delta(t)$ is the Dirac delta function. However this assumption is not necessary as we showed above and we can use P waves that do not impinge so steeply.

2.1.1 Observed Receiver Function

We call a receiver function obtained from an observed waveform an 'observed' receiver function because it appears as an observation term in observation equations in our inversions.

The data used in this study are observed by using STS seismometers that have wide dynamic range (140dB) and very broad band ($0.1 \sim 360$ s). The details of our observation system are written in Shibutani et al. (1990).

We obtain receiver functions from P waveforms of nearby deep earthquakes with magnitude greater than 5. Since the dominant frequencies of the P waves nearby deep events are higher than those of teleseismic events, using the regional receiver functions might have potential to resolve finer structure than teleseismic receiver functions. However higher frequency receiver functions contain more scattered energy due to small scale heterogeneities, so there is a risk that they would lead to an overly complicated one-dimensional velocity estimate. We examined frequency content of the P waveforms by spectrum analysis and estimated the upper limit of the frequency we can use in the receiver functions at 0.5 Hz (Shibutani 1993). Therefore we restrict the frequency content of the receiver functions by low-pass-

filtering the original waveforms with the corner frequency of 0.5 Hz. And we set $\alpha = 3$ in the above Gaussian high cut filter in the eq. (4) so that frequencies of the receiver functions are limited up to 0.5 Hz. In this case wavelengths of the incident P waves are longer than $3 \sim 4$ km. The layer thickness of our horizontally stratified velocity structure model is set to be 2 km, so that the layers should influence the receiver function noticeably because the relation, $\lambda/4 < \delta$, holds true between the wavelength (λ) and the layer thickness (δ). We checked the inversion for other layer thickness, that is 1.5 km and 2.5 km, however, in both cases the rms residuals between the observed and synthetic radial receiver functions are larger than those in the case of the thickness of 2.0 km. The parameter c is set to be 0.00001 in all cases.

We use the absolute amplitude of receiver functions and it makes the receiver function inversion technique robust especially in modeling shallower regions as examined by Ammon (1991) and Cassidy (1992).

2.1.2 Synthetic Receiver Function

We calculate the response of given earth structure models, $E_V(\omega)$, $E_R(\omega)$ and $E_T(\omega)$ using a Thomson-Haskell method (Haskell 1962) and then obtain synthetic receiver functions using eqs.(2), (3) and (4) with replacing $D_V(\omega)$, $D_R(\omega)$ and $D_T(\omega)$ by $E_V(\omega)$, $E_R(\omega)$ and $E_T(\omega)$, respectively. The same α and c are used as in observed receiver functions. The incident angles of the P waves are estimated by ray tracing in each source-station pair.

Figure 1: Synthetic radial receiver functions.

Figure 2: Ray diagram of major phases in radial receiver functions.

Fig. 1 shows synthetic radial receiver functions that are calculated for the two-layer-model shown in Fig. 2 in two cases with incident angle of 25° and 40° The

ray paths of the major phases in the radial receiver functions named such as Pp, Ps etc. are shown in Fig. 2. We can find from both figures that the major phases except the direct P wave (Pp) in the radial receiver functions are P-to-S converted waves at the interface.

2.2 Linearized Time Domain Inversion

Since the tangential receiver function is not generated theoretically in the case of an incident P wave to horizontally stratified layers, we will invert only the radial receiver function in this study.

According to Owens et al. (1984), the best approach is to invert the radial receiver functions only for S wave velocity model consisting of horizontal layers of fixed thickness since the radial receiver functions are most sensitive to the S wave velocity. We checked this by differential radial receiver functions due to the three possible model parameters' perturbation and obtained the same result as Owens et al. (1984) (Shibutani 1993). We adjust P wave velocity (V_P) assuming $V_P/V_S = 2.00$ for the first layer, 1.80 for the second layer, 1.73 for the upper and lower crust and 1.80 for the uppermost mantle, where V_S is S wave velocity and use the relationship between density (ρ) and the P wave velocity: $\rho = 2.35 + 0.036\,(V_P - 3.0)^2$ (Kurita 1973). We assume fixed Q values in each layer, that is $Q_\alpha = 225$, $Q_\beta = 100$ for the first layer, $Q_\alpha = 675$, $Q_\beta = 300$ for the second layer, $Q_\alpha = 1450$, $Q_\beta = 600$ for the crust and $Q_\alpha = 340$, $Q_\beta = 150$ for the mantle, where Q_α and Q_β are the Q value for P wave and S wave, respectively. However the Q values scarcely effect the receiver functions. We also assume the velocity structure to be isotropic.

2.2.1 Multi-trace Inversion

The observation equation for the i-th time point and the j-th trace can be expressed as follows:

$$r_i^j = R_i^j(\pi n) \tag{5}$$

where r_i^j is the observed radial receiver function; R_i^j is the synthetic radial receiver function; and $\boldsymbol{m} = (m_1, m_2, \cdots, m_M)^T$ is the velocity model (a M-dimensional vector).

After linearizing the eq.(5), we have

$$(G^j \, \delta m)_i = r_i^j - R_i^j(m_0) \tag{6}$$

where G^j is the partial derivative matrix of the j-th radial receiver function whose (i,k)-component is expressed by

$$G_{ik}^j = \frac{\partial R_i^j}{\partial m_k}; \tag{7}$$

m_0 is the initial velocity model; and δm is the model correction vector. Adding the inner product $(G^j \, m_0)_i$ to both sides of eq. (6), it becomes

$$(G^j \, m)_i = r_i^j - R_i^j(m_0) + (G^j \, m_0)_i \, . \tag{8}$$

Putting $d_i^j = r_i^j - R_i^j(m_0) + (G^j \, m_0)_i$, $d^j = (d_1^j, d_2^j, \cdots, d_N^j)^T$, $G = (G^1, G^2, \cdots, G^L)^T$ and $d = (d^1, d^2, \cdots, d^L)^T$, eq. (8) is written in matrix form as

$$G \, m = d \, . \tag{9}$$

2.2.2 Smoothness Constraint

According to Ammon, Randall and Zandt (1990), we implement a smoothness constraint in our inversions by minimizing a roughness norm of the velocity model. To accomplish this, we introduce the matrix Δ which constructs the second difference of the model m, that is,

$$\Delta = \begin{pmatrix} 1 & -2 & 1 & 0 & \cdots \\ 0 & 1 & -2 & 1 & \cdots \\ 0 & 0 & 1 & -2 & \cdots \\ 0 & 0 & 0 & 1 & \cdots \\ \vdots & \vdots & \vdots & \vdots & \ddots \end{pmatrix},$$

and alter eq. (9) to

$$\begin{pmatrix} G \\ \sigma \, \Delta \end{pmatrix} m = \begin{pmatrix} d \\ \mathrm{o} \end{pmatrix} \tag{10}$$

Then the least square solution of eq. (10) can be written as

$$\widehat{\boldsymbol{m}} = (\boldsymbol{G}^T \boldsymbol{G} + \sigma^2 \boldsymbol{\Delta}^T \boldsymbol{\Delta})^{-1} \boldsymbol{G}^T \boldsymbol{d}, \tag{11}$$

which is identical to the damped least square solution with a damping factor of $\sigma^2 \boldsymbol{\Delta}^T \boldsymbol{\Delta}$. We can control the trade-off between fitting the waveform and smoothness of the model by adjusting the parameter σ.

The resolution matrix $\boldsymbol{R}$ can be expressed as

$$\boldsymbol{R} = (\boldsymbol{G}^T \boldsymbol{G} + \sigma^2 \boldsymbol{\Delta}^T \boldsymbol{\Delta})^{-1} \boldsymbol{G}^T \boldsymbol{G}, \tag{12}$$

and the error in the model $\boldsymbol{m}$ can be estimated as

$$< \Delta\widehat{\boldsymbol{m}} \, \Delta\widehat{\boldsymbol{m}}^T >= \sigma_d^2 (\boldsymbol{G}^T \boldsymbol{G} + \sigma^2 \boldsymbol{\Delta}^T \boldsymbol{\Delta})^{-1} \boldsymbol{R}, \tag{13}$$

where the variance of data σ_d^2 can be estimate as

$$\frac{[\sum (\text{O-C})^2]}{[\text{degree of freedom}]}.$$

See Aki and Richards (1980), Vol.II, p.694. Note that Δ in eq. (13) means error in $\widehat{\boldsymbol{m}}$ and is different from the second-difference matrix $\boldsymbol{\Delta}$.

3 RESULTS

In this study we analyzed P waveforms of deep earthquakes near Honshu, Japan, which are listed in Table 1. The depths of the hypocenters range from 321 $\sim$ 529 km. The epicenters of the events and the location of the station TTT are shown in Fig. 3. The station TTT is located in an active fault zone in the Inner zone of Southwest Japan and near the epicenter of Tottori earthquake of 1943, which was a large inland strike-slip event with a magnitude of 7.2.

Table 1: Location of TTT and its events

In Figs. 4 and 5, radial and tangential receiver functions are lined up in order of backazimuth clockwise from the north, respectively. The peaks at $t = 0$ s in

each trace of the radial receiver functions indicate the direct P arrivals and the later phases are considered P-to-S converted waves at discontinuities in the earth's interior as illustrated in Figs. 1 and 2.

Figure 3: Location of TTT and its events

We can find interesting facts from Fig. 4 that radial receiver functions with close backazimuths have similar waveforms, especially during the first 15 s, for examples, in the cases of T0023, T0164, T0156 and T0211, and in the cases of T0009 and T0493. Although the backazimuthes of T0346 and T0067 are close to those of the first group, their radial receiver functions are not so similar to those in the group. This can be explained by that the two receiver functions might be seriously contaminated by noises because the rms amplitude ratio between the tangential and the radial component for them are relatively large (See the column of T/R in Table 1). On the contrary, radial receiver functions with backazimuths of more than 10° have few common phases. This suggests that there are lateral heterogeneities in the structure beneath TTT but that the structure does not change so much in the azimuthal range of about 10°.

Figure 4: Observed radial receiver functions for TTT

Figure 5: Observed tangential receiver functions for TTT

On the other hand, Fig. 5 indicates in general that the tangential receiver functions have smaller amplitudes and less correlated waveforms compared with the radial receiver functions. Although the tangential receiver functions of T0009 and T0493 resemble well each other, their amplitudes are only 20 $\sim$ 25 % of those of the radial receiver functions. We calculate the radial and the tangential component referred to a backazimuth derived from a particle motion of the first swing of P wave. A possible reason why some tangential receiver functions have similar waveforms is

that they are formed from off-azimuthal P incident waves that are generated by P-to-S converted waves at dipping interfaces or scattered waves due to rather large-scale heterogeneities.

We selected four traces of the radial receiver functions of T0023, T0164, T0156 and T0211 for a model along an S50°E backazimuth and two traces of T0009 and T0493 for a model along an S30°E backazimuth with following reasons.

1. They have very similar waveforms as mentioned above. Their backazimuths are within the range of 13° and the incident angles of their P waves vary within 10°. Shibutani (1993) indicated that the multi-trace inversion using radial receiver functions corresponding to different incident angles by 10° in maximum can give us a better final model than the single-trace inversion using a stacked radial receiver function. However if the incident angles are so different that the incident P waves sample different regions, the correlation of waveforms among the receiver functions might be inadequate. Flatté and Wu (1988) investigated the statistical distribution of heterogeneities in the lithosphere and asthenosphere using NORSAR array data. Their results indicate that the correlation of amplitude and phase among waveforms becomes very small if the difference among their incoming angles is larger than 10°. So we selected the receiver functions which have similar waveforms among those which are satisfied with the above conditions.

2. The rms amplitude ratio of the tangential receiver function to the radial receiver function for these events is small, less than 50 %. Since our modeling is one-dimensional, horizontally stratified structure, we have no tangential energy in the receiver function theoretically. Therefore we cannot use the receiver functions whose tangential component has large energy. According to our numerical experiments (Shibutani 1993), the allowable upper limit of the rms amplitude ratio is 60 %.

In fact the receiver functions are different in details. This may be because the

observed waveforms are contaminated by background noises and scattered waves due to small scale heterogeneities. However if we invert these receiver functions together for one model, we can obtain a model which reflects common factors among the receiver functions.

3.1 An S wave velocity model along an S50°E backazimuth: Model S50E-1

An initial model is illustrated in Fig. 6 by the dotted line that is based on the previous refraction and reflection studies by Yoshii et al. (1974). We try a few more initial models and compare the waveform fit between the observed and synthetic receiver functions. Then we adopted the final model that have smaller residual on the whole and better waveform fit for characteristic phases. Effect of initial models on final models will be discussed in detail in the section 4.1.

Figure 6: S wave velocity model : S50E-1

As mentioned in the section 2.2.2, the smoothness parameter σ controls the trade-off between the waveform fit and model smoothness or model roughness. The model roughness is calculated by

$$\text{roughness} = \sum_{i=1}^{n-2} \frac{|\beta_i - 2\beta_{i+1} + \beta_{i+2}|}{n-2} \tag{14}$$

where β_i is the S wave velocity of the ith layer and n is the total number of layers in the velocity model. We chose a smoothness parameter of 0.4 for the model S50E-1. In this case the model roughness is 0.28, the rms residual is 0.069 and the average resolution is 0.80 with the worst resolution of 0.69 at the 27-th layer.

Figure 7: Waveform fit for S50E-1

Figure 8: Differential radial receiver functions for the final model S50E-1

The final model resulting with $\sigma = 0.4$ is shown in Fig. 6 by the solid line with error bars estimated by using eq. (13). The waveform fit between observed and synthetic radial receiver functions for the events of T0023, T0164, T0156 and T0211 are shown in Fig. 7. And Fig. 8 shows differential radial receiver functions for the final model S50E-1 that represent how P-to-S converted waves are generated in a radial receiver function if the S wave velocity in a layer is perturbed. The up and the down swings seen in the waveforms of Ps and $PpPds$ are generated at the upper and the lower interface of the perturbed layer, respectively. The phases seen at 12.5 s in a depth range of $2 \sim 30$ km are due to the $PpPms$ phase. The synthetic waveform are in good agreement with the observed in a time window of $0 \sim 20$ s. The features of the final model S50E-1 are summarized as follows:

1. The final model is much more complicated than the initial model which is based on the previous study by Yoshii et al. (1974). However the three major discontinuities at the top of the upper crust, the lower crust and the uppermost mantle also exist in the final model at the same depth as in the initial model.

2. The first layer in the surface layer has a low S wave velocity of 2.8 km/s. The velocity jumps to increase to 3.4 km/s in the second layer. The velocity structure of the surface layer is controlled by the first 5 s of the receiver functions as shown in Fig. 8. And it suggests that the first layer is unsolidified but the second layer is almost solidified so that it has a velocity close to one in the upper crust.

3. The layers in the depths of $16 \sim 28$ km which correspond to the lower crust have a structure of alternate high and low velocity. The structure in these depths is constrained by multiplets in the radial receiver functions in a time window of $5 \sim 10$ s. The lower crust has been revealed to be highly reflective for both P and S waves by a number of studies (e.g. Klemperer 1987, Lüschen et al. 1987, Mooney and Brocher 1987, Goodwin and McCarthy 1990). And it is explained by laminar structure of alternate high and low velocity whose

thickness is 100 $\sim$ 200 m which is considered to be related to fluidity of the lower crust. The alternate velocity change seen in our final model might be macroscopic manifestation of the microscopic structure in the lower crust.

4. The most striking feature is a high velocity layer between 32 $\sim$ 34 km with S wave velocity of 4.9 km/s. The corresponding P-to-S converted waves can be seen around 4.3 s (Ps) and 12.5 s ($PpPms$) and the waveform fit between the observed and synthetic receiver functions is pretty well. A high velocity layer corresponding this one is also obtained in a velocity model along an S30°E backazimuth as mentioned latter. The Moho discontinuity might be the top of this high velocity layer or exist at a depth of 30 km.

5. The velocities in the uppermost mantle below the high velocity layer change more gradually than in the shallower depths. There are a high velocity zone in the depths of 44 $\sim$ 52 km and a low velocity zone in the depths of 54 $\sim$ 58 km.

The reason why the waveform fit is not good after 20 s is that, as shown in Fig 8, the $PpSds$ is the only converted phase in the time window and the amplitude of the phase is much smaller than that of the Ps and $PpPms$ phases and that the velocity model is mainly constrained by the latter two phases in the receiver function inversions.

3.2 An S wave velocity model along an S30°E backazimuth : Model S30E-1

Figure 9: S velocity model : S30E-1

Figure 10: Waveform fit for S30E-1

For the velocity model S30E-1, two traces of T0009 and T0493 are inverted with the same initial model as in the model S50E-1. In this case we chose a smoothness

parameter of 0.2, as the result, the model roughness is 0.29, the rms residual is 0.056 and the average resolution is 0.86 with the worst resolution of 0.73 in the 30-th layer. The corresponding final model are shown in Fig. 9 by the solid line with error bars. Fig. 10 shows the waveform fit between the observed and synthetic radial receiver functions for the events of T0009 and T0493. They are in good agreement with each other in a time window of $0 \sim 20$ s. The features are as follows:

1. Relative velocity changes resemble well with each other between this models and S50E-1, especially in the shallow layers (~ 6 km), the upper part of the lower crust ($16 \sim 24$ km) and the high velocity layer ($32 \sim 34$ km).

2. The absolute velocities in the upper crust are lower than in S50E-1 by $0.1 \sim 0.3$ km/s, while those in the lower crust are the same in both models. The absolute velocity in the high velocity layer is 4.6 km/s, smaller than that in S50E-1 by 0.3km/s.

3. The depths of $42 \sim 50$ km form a low velocity zone, while the corresponding depths form a high velocity zone in the model S50E-1.

4 DISCUSSIONS

4.1 Effect of initial models on final models

As mentioned above in the section of 3, we tried to invert a set of radial receiver functions by starting with several different initial models, and compared the final models to investigate effect of the initial models on the final models.

Figure 11: Three initial models for S50E for a test on the nonuniqueness of our inversion

Figure 12: The corresponding final models for S50E

Figs. 11 and 12 show initial models and the corresponding final models, respectively, for the case of inverting radial receiver functions of T0023, T0164, T0156 and

T0211. The initial model of S50E-2 is based on the previous refraction study by Sasaki et al. (1970) which has a thicker lower crust and a lower S wave velocity of the lower crust than the initial model of S50E-1. The initial model of S50E-3 is a extreme case in which the S velocity gradually increases with depth without any major discontinuity. We chose the final model S50E-1 as the best model of TTT because for the model the observed and synthetic receiver functions have more similar waveforms for characteristic phases and the rms residual is smaller on the whole than for the other models. The corresponding final models are shown in Fig. 12. They resemble each other on the whole. However significant differences are seen in the lower crust and at the Moho discontinuity. We found a feature that in the model whose Moho discontinuity is determined deeper, the average velocity of the lower crust is higher. This suggests that the velocity in the layers around the Moho discontinuity and that in the lower crust compensate each other in travel times of P-to-S converted waves relative to the direct P wave.

Ammon et al. (1990) investigated the nonuniqueness of the receiver function inversion, and indicated that the primary sensitivity of receiver function inversions is to high wave-number velocity changes, and a depth-velocity product, not simply velocity. In other words, high wavenumber velocity variations are well resolved, but broad velocity variations are not well constrained, and a substantial trade-off exists between the average velocity above a discontinuity and the depth of it. These features of the nonuniqueness are also seen in our inversions. For instance, in the case of S50E we found a trade-off between the depth of the Moho discontinuity and the velocity of the lower crust above the Moho.

To reduce such uncertainties in the final models, it is necessary to apply a priori informations such as a velocity in shallow layers derived from a refraction study to initial models as pointed out by Ammon et al. (1990). Our initial models of S50E-1, S50E-2 and S30E-1 are mainly based on the previous refraction studies, and the extreme models of S50E-3 are formed in such a manner that the way of velocity increase down to the Moho is equal to the trend of velocity increase in the other

models. The agreement in the general velocity structure among the final models suggests that our receiver function inversion has ability to determine an appropriate velocity model on the whole if only an initial model with a proper structure in average is given.

In a case where an initial model has a false discontinuity different significantly in depth and/or velocity, the corresponding final model would be significantly different from the most suitable model. However in such a case we can obtain a suitable model by using our inversion iteratively. This situation is illustrated in Figs. 13 and 14.

Figure 13: Three initial models for S50E for a test on an iterative inversion

Figure 14: The corresponding final models for S50E

The initial model S50E-4A in Fig. 13 has a false Moho discontinuity at a depth of 40 km. The corresponding final model in Fig. 14 is significantly different from the best model S50E-1. However in the final model S50E-4A the Moho discontinuity exists at a depth of 30 km, not 40 km. Then we changed the initial model to S50E-4B and made a inversion again. The resulting final model S50E-4B in Fig. 14 is in good agreement with S50E-1.

4.2 Problems in observed receiver functions

We notice presignal noises with considerable amplitude in some radial receiver functions in Fig. 4. These presignal noises are thought to be due to background noises such as microtremors generated by waves, wind or activity of human beings. Since they are not taken into consideration in the forward modeling, inversions of receiver functions strongly contaminated by them would mislead us to false final models. However the amplitude of the presignal noises in the radial receiver functions we used in our inversions are considerably small compared with that of the signals, and we find from Fig. 4 that the presignal noises do not have good correlation with

each other. So if we invert several receiver functions simultaneously, we can obtain a final model that are not much influenced by the background noises, because the final model would reflect common phases among the receiver functions. We now make numerical experiments to estimate the effects of the background noises on final models. The results are shown in our paper written in parallel (Shibutani 1993).

We also notice in Fig. 5 that the tangential receiver functions have considerable energy. These tangential components can be generated by the background noises mentioned above, P-to-S converted waves at dipping interfaces and scattered waves from various scales of heterogeneities. Then the radial receiver functions are also contaminated by these waves. Since we model the earth's interior as horizontally stratified layers, the P-to-S converted waves at dipping interfaces and the scattered waves would also mislead us to false final models as well as the background noises.

Cassidy (1992) estimated the effects of dipping interfaces on the radial and tangential receiver functions. His results indicate that the receiver functions exhibit drastic variations in amplitude and arrival times as a function of backazimuth and incident angle in the presence of dipping interfaces.

By inverting several receiver functions simultaneously we can reduce the erroneous effects of those waves on the final models, but cannot eliminate them perfectly. We should rather develop a method to obtain 2-D models for dipping interfaces or 3-D models for small scale heterogeneities by using both radial and tangential receiver functions. This is our future problem.

5 CONCLUSIONS

We developed a new method called 'multi-trace receiver function inversion' and inverted regional receiver functions derived from P waveforms of nearby deep earthquakes south off Honshu, Japan. The receiver function inversion was successfully applied and vertical velocity structure models of S wave for two backazimuths of S50°E and S30°E beneath TTT were obtained. They consist of 31 layers with

thicknesses of 2 km, hence they are very minute compared with models acquired by previous works such as refraction studies. Therefore we can discuss subtle structures in the upper and lower crust and the uppermost mantle.

The P waveforms of ten deep events were analyzed in this study. The radial receiver functions with close backazimuths have similar waveforms but those with backazimuths of greater than 10° have few common phases. On the other hand, the tangential receiver functions have smaller amplitudes and less correlated waveforms compared with the radial receiver functions. This suggests that there are lateral heterogeneities beneath the stations but the structure does not change so much in the azimuthal range of 10°.

The final models of S50E-1 and S30E-1 that gives the S velocity structure for two backazimuths of S50°E and S30°E beneath TTT is in rough agreement with the initial model in the depth of the major discontinuities, although they are much more complicated than their initial models. The main features in the final models are that the S wave velocity in the first layer is very small, that the upper part of the lower crust has a structure of alternate high and low velocity and that there is a high velocity layer at the top of the Moho discontinuity.

To investigate the nonuniqueness of our inversion, we inverted a set of receiver functions with several different initial models and compared the resulting final models. They are in good agreement with each other in the overall structure. Thus our inversion can determine an appropriate model if only a proper velocity structure in average is given as an initial model.

The existence of presignal noises in radial receiver functions and some energy in tangential receiver functions indicates that the background noises and the scattered energy from various scales of heterogeneities contaminate the receiver functions. So there would be a risk for us to be misled to a false velocity model if we would invert receiver functions strongly contaminated by such noises. We now numerically simulate the effect of the background noises on the final models. The result will be shown in our paper written in parallel (Shibutani 1993). Furthermore another approach

should be made in which both of the radial and tangential receiver functions are inverted for 2-D or 3-D velocity models. This attempt is our future problem.

ACKNOWLEDGMENTS

I thank Dr. Kazuro Hirahara. It was he that introduced the paper by Owens et al. (1984) to me. And he guided me on inversion theory and gave me a prototype program of inversion. I could make many fruitful discussions with him. I thank Prof. Kazuo Oike who gave me an opportunity to make broadband seismic observations with the STS seismometers. He also encouraged me through my work. I thank Prof. Masataka Ando and Dr. Fumiaki Takeuchi for their advice and encouragement. I also thank Dr. Takeshi Mikumo for allowing me to use his computer program of Thomson-Haskell method. I thank Mr. Setsuro Nakao in Tottori Observatory, Mr. Hiroo Wada in Kamitakara Observatory and Mr. Norio Hirano in Hokuriku Observatory, who maintain the observations with the STS seismometers. The comments of two anonymous reviewer are also gratefully acknowledged. Calculations were carried out at the Data Processing Center, Kyoto University.

REFERENCES

Aki, K. & Richards, P. G., 1980. Quantitative Seismology, Theory and Methods, Volume II, W. H. Freeman, San Francisco.

Ammon, C. J., Randall, G. E. & Zandt, G., 1990. On the nonuniqueness of receiver function inversions, J. Geophys. Res., **95**, 15,303–15,318.

Ammon, C. J., 1991. The isolation of receiver effects from teleseismic P waveforms, Bull. Seism. Soc. Am., **81**, 2,504–2510.

Cassidy, J. F., 1992. Numerical experiments in broadband receiver function analysis, Bull. Seism. Soc. Am., **82**, 1,453–1,474.

Flatté, S. M. & Wu, R. S., 1988. Small-scale structure in the lithosphere and asthenosphere deduced from arrival time and amplitude fluctuations at NORSAR, J. Geophys. Res., **93**, 6601–6614.

Goodwin, E. B. & McCarthy, J., 1990. Composition of the lower crust in west central Arizona from three-component seismic data, J. Geophys. Research, **95**, 20,097–20,109.

Hashizume, M., Kawamoto, O., Asano, S., Muramatu, I., Asada, T., Tamaki, I. & Murauchi, S., 1966. Crustal structure in the western part of Japan derived from the observation of the first and second Kurayoshi and the Hanabusa explosions, Part 2. Crustal structure in the western part of Japan, Bull. Earthq. Res. Inst., **44**, 109–120.

Haskell, N. A., 1962. Crustal reflection of plane P and SV waves, J. Geophys. Res., **67**, 4751–4767.

Klemperer, S. L., 1987. A relation between continental heat flow and the seismic reflectivity of the lower crust, J. Geophys., **61**, 1–11.

Kurita, T., 1973. Regional variations in the structure of the crust in the central United States from *P*-wave spectra, Bull. Seism. Soc. Am., **63**, 1663–1687.

Langston, C. A., 1979. Structure under Mount Rainier, Washington, inferred from teleseismic body waves, J. Geophys. Res., **84**, 4,749–4,762.

Lüschen, E., Wenzel, F., Sandmeier, K. J., Menges, D., Rühl, Th., Stiller, M., Janoth, W., Keller, F., Söllner, W., Thomas, R., Krohe, A., Stenger, R., Fuchs, K., Wilhelm, H. & Eisbacher, G., 1987. Near-vertical and wide-angle seismic surveys in the Black Forest, SW Germany, J. Geophys., **62**, 1–30.

Mooney, W. D., Brocher, T. M., Coincident seismic reflection/refraction studies of the continental lithosphere: A global review, Rev. Geophysics, **25**, 723–742.

Owens, T. J., Zandt, G. & Taylor, S.R., 1984. Seismic evidence for an ancient rift beneath the Cumberland Plateau, Tennessee: A detailed analysis of broadband teleseismic *P* waveforms, J. Geophys. Res., **89**, 7783–7795.

Owens, T. J., 1987. Crustal structure of the Adirondacks determined from broadband teleseismic waveform modeling, J. Geophys. Res., **92**, 6,391–6,401.

Sasaki, Y., Asano, S., Muramatu, I., Hashizume, M. & Asada, T., 1970. Crustal structure in the western part of Japan derived from the observation of the first and second Kurayoshi and the Hanabusa explosions (continued), Part 2. Crustal structure in the western part of Japan (continued), Bull. Earthq. Res. Inst., **48**, 1129–1136.

Shibutani, T., Oike, K., Hirahara, K., Nishigami, K., Wada, H., Nakao, S. & Hirano, N., 1990. Seismic observation with high-performance seismometers (STS) — Introduction of observation system and examples of seismic waveform, Annu. Disas. Prev. Res. Inst., Kyoto Univ., **33B-1**, 39–56 (in Japanese with English abstract).

Shibutani, T., 1993. Numerical experiments on the multi-trace receiver function inversion to estimate S wave velocity structure of the crust and uppermost mantle, submitted to Geophys. J. Int.

Yoshii, T., Sasaki, Y., Tada, T., Okada, H., Asano, S., Muramatu, I., Hashizume, M. & Moriya, T., 1974. The third Kurayoshi explosion and the crustal structure in the western part of Japan, J. Phys. Earth, 22, 109–121.

Figure Captions

Figure 1 Synthetic radial receiver functions that are calculated for the two-layer-model illustrated in Fig. 2. The solid and dotted lines indicate the cases where the incident angle of P wave is 40° and 25°, respectively. The major phases such as Pp, Ps, etc. are illustrated in Fig. 2. Note that the amplitude of the major phases in the case of the incident angle of 40° are larger than that in the case of the incident angle of 25°.

Figure 2 Simple two-layer-model for which the radial receiver functions in Fig. 1 are calculated and simplified ray diagram showing the major P-to-S converted waves that make up the radial receiver functions.

Figure 3 Map showing the station of TTT (triangle) and the nearby deep events analyzed in this study (asterisks). Their parameters are listed in Table 1.

Figure 4 Radial receiver functions derived from P waveforms of nearby deep events observed at TTT. They are aligned at the direct P phase and lined up in order of backazimuth clockwise from the north.

Figure 5 Tangential receiver functions derived from P waveforms of nearby deep events observed at TTT. They are aligned at the direct P phase and lined up in order of backazimuth clockwise from the north.

Figure 6 S wave velocity model S50E-1 along an S50°E backazimuth for the station of TTT. The dotted line indicates the initial model. The solid line indicates the final model obtained by inverting the four radial receiver functions shown by the dotted line in Fig. 7. Errors in the S wave velocity of each layer are indicated with the bars.

Figure 7 Observed (dotted lines) and synthetic (solid lines) radial receiver functions for the four events: T0023, T0164, T0156 and T0211. The synthetic

receiver functions are calculated for the final model of S50E-1 shown by the solid line in Fig. 6. i denotes the incident angle of P wave used in the calculation of the synthetic receiver functions.

Figure 8 Differential radial receiver functions in the case of P wave incidence to the final model of S50E-1 with the incident angle of 47.5°. The differential receiver function can be expressed by eq. (7) and represents effects of velocity perturbation in a layer on a radial receiver function.

Figure 9 S wave velocity model S30E-1 along an S30°E backazimuth for the station of TTT. The dotted line indicates the initial model. The solid line indicates the final model obtained by inverting the two radial receiver functions shown by the dotted line in Fig. 10. Errors in the S velocity of each layer are indicated with the bars.

Figure 10 Observed (dotted lines) and synthetic (solid lines) radial receiver functions for the two events: T0009 and T0493. The synthetic receiver functions are calculated for the final model of S30E-1 shown by the solid line in Fig. 9. i denotes the incident angle of P wave used in the calculation of the receiver functions.

Figure 11 Three initial models for a test on the nonuniqueness of our inversion. The models S50E-1 and S50E-2 are based on the previous study by Yoshii et al. (1974) and Sasaki et al. (1970),respectively. And the model S50E-3 is formed in such a manner that the way of velocity increase down to the Moho is equal to the trend of velocity increase in the other models.

Figure 12 The corresponding final models to the initial models shown in Fig. 11.

Figure 13 Three initial models for a test on an iterative inversion. The model S50E-4A are based on the previous study by Sasaki et al. (1970), and the model S50E-4B is modified based on the final model of S50E-4A.

Figure 14 The corresponding final models to the initial models shown in Fig. 13.

Table 1. Location of TTT and events analyzed in this study

Station	Lat. N°	Lon. E°	Height m
TTT	35.5147	134.2378	10.0

Events	Lat. N°	Lon. E°	Depth km	Distance km	Backazimuth deg	M_{JMA}	T/R	Date
T0136	36.993	134.665	396.1	168.5	13.05	5.5	0.55	Mar. 21, 1989
T0383	35.517	135.642	367.9	127.4	89.48	6.4	1.05	Apr. 12, 1990
T0346	34.502	136.443	371.2	230.5	118.53	5.5	0.85	Jan. 31, 1990
T0067	33.582	138.112	321.3	415.2	119.98	5.7	0.85	Nov. 14, 1991
T0023	33.847	137.260	363.1	333.0	122.88	5.3	0.45	Aug. 08, 1988
T0164	33.463	139.933	401.0	336.3	131.83	5.7	0.38	June 04, 1989
T0156	32.378	137.840	410.4	481.5	135.24	5.9	0.32	May 09, 1989
T0211	32.528	137.647	419.4	457.0	135.49	5.8	0.50	Aug. 03, 1989
T0009	30.270	137.785	513.6	669.5	149.31	6.8	0.24	Sep. 07, 1988
T0493	29.457	138.005	529.0	759.2	151.18	6.7	0.18	Aug. 05, 1990

M_{JMA} denotes the earthquake magnitude determined by Japan Meteorological Agency.

T/R is the rms-amplitude ratio of the tangential to the radial component of a receiver function.

Date refers to Japan Standard Time.

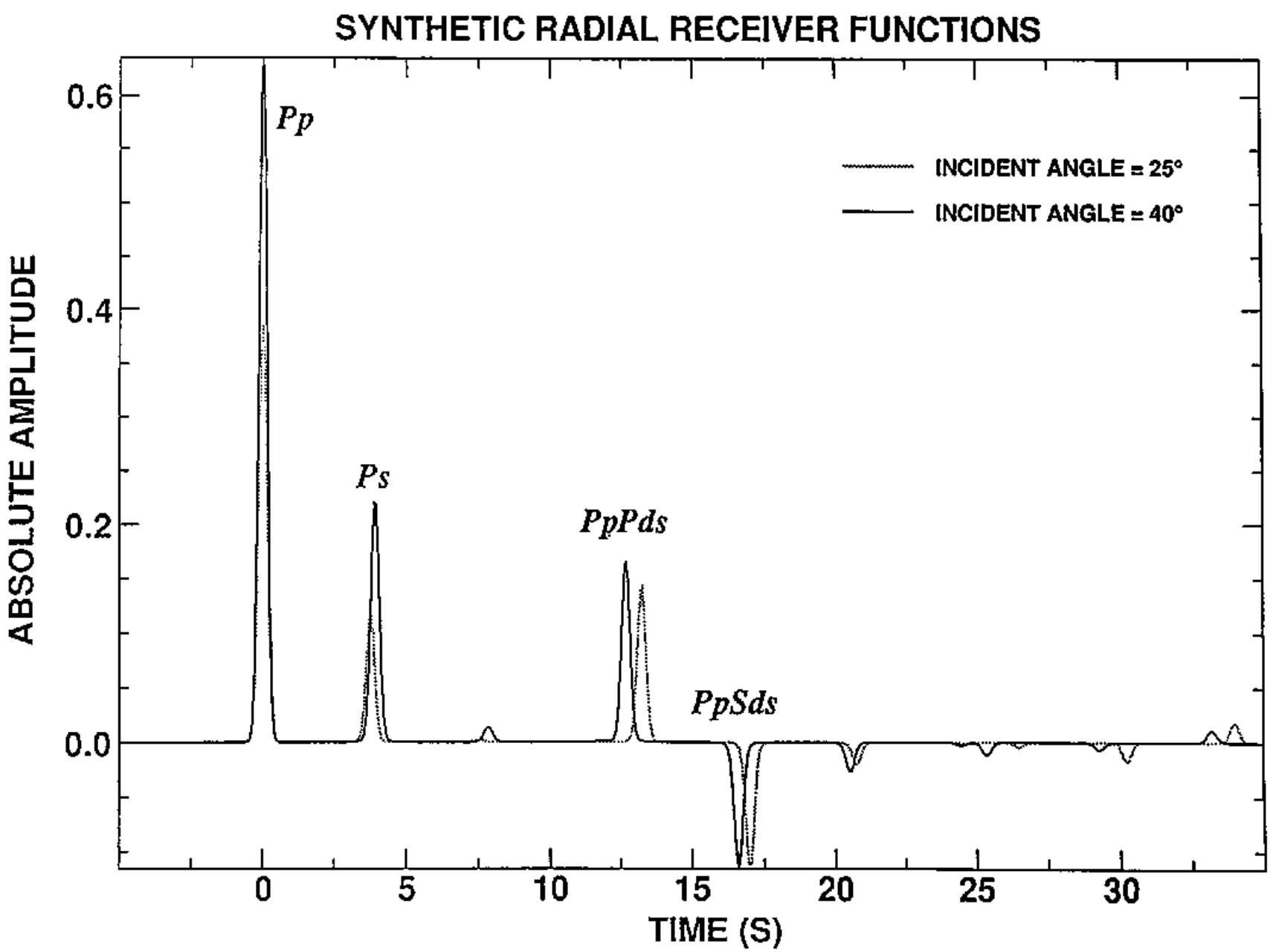
SYNTHETIC RADIAL RECEIVER FUNCTIONS
ABSOLUTE AMPLITUDE
0.6
0.4
0.2
0.0
Pp
Ps
PpPds
PpSds
INCIDENT ANGLE = 25°
INCIDENT ANGLE = 40°
0
5
10
15
20
25
30
TIME (S)

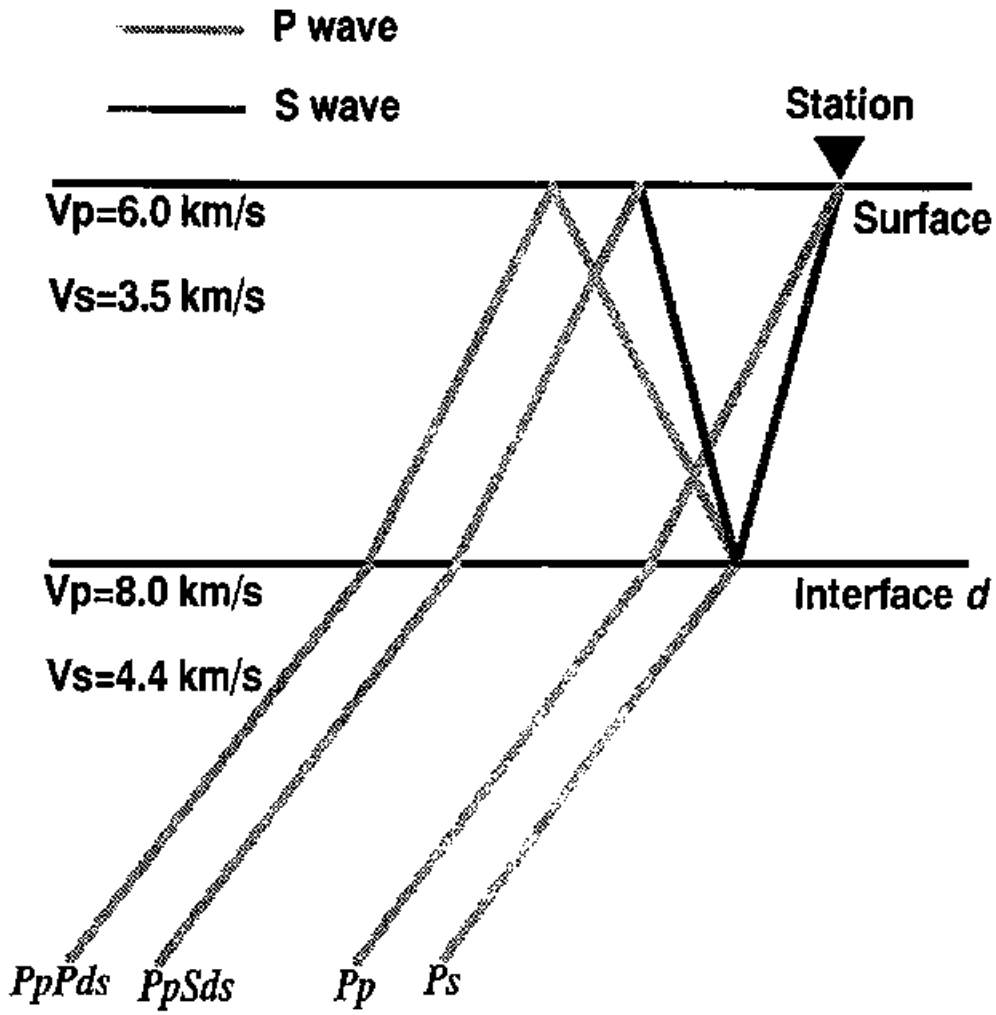
P wave
S wave
Station
Vp=6.0 km/s
Vs=3.5 km/s
Surface
Vp=8.0 km/s
Vs=4.4 km/s
Interface d
PpPds
PpSds
Pp
Ps

Figure 2

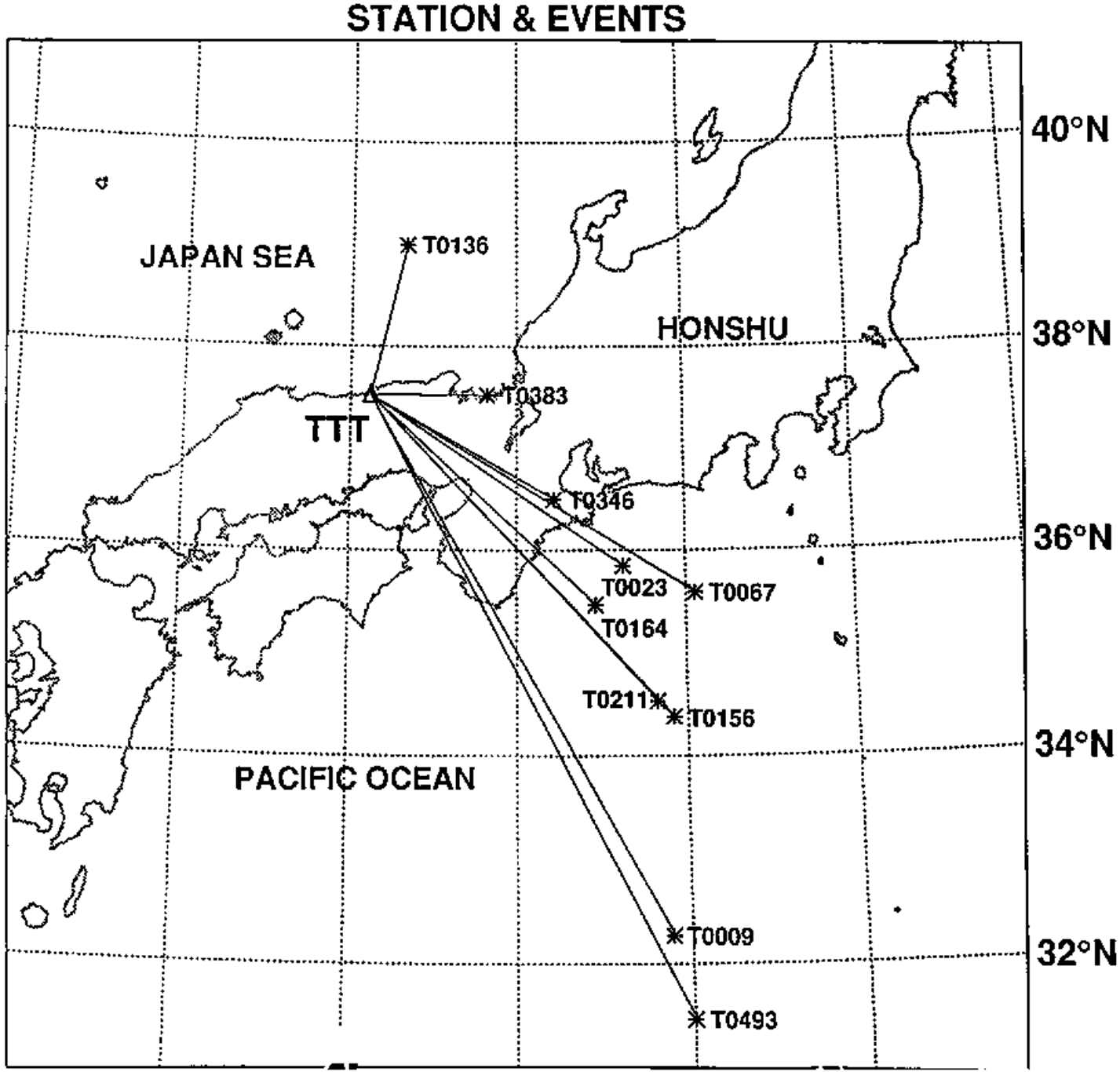
STATION & EVENTS
JAPAN SEA
HONSHU
PACIFIC OCEAN
TTT
T0136
T0383
T0346
T0023
T0067
T0164
T0211
T0156
T0009
T0493
40°N
38°N
36°N
34°N
32°N

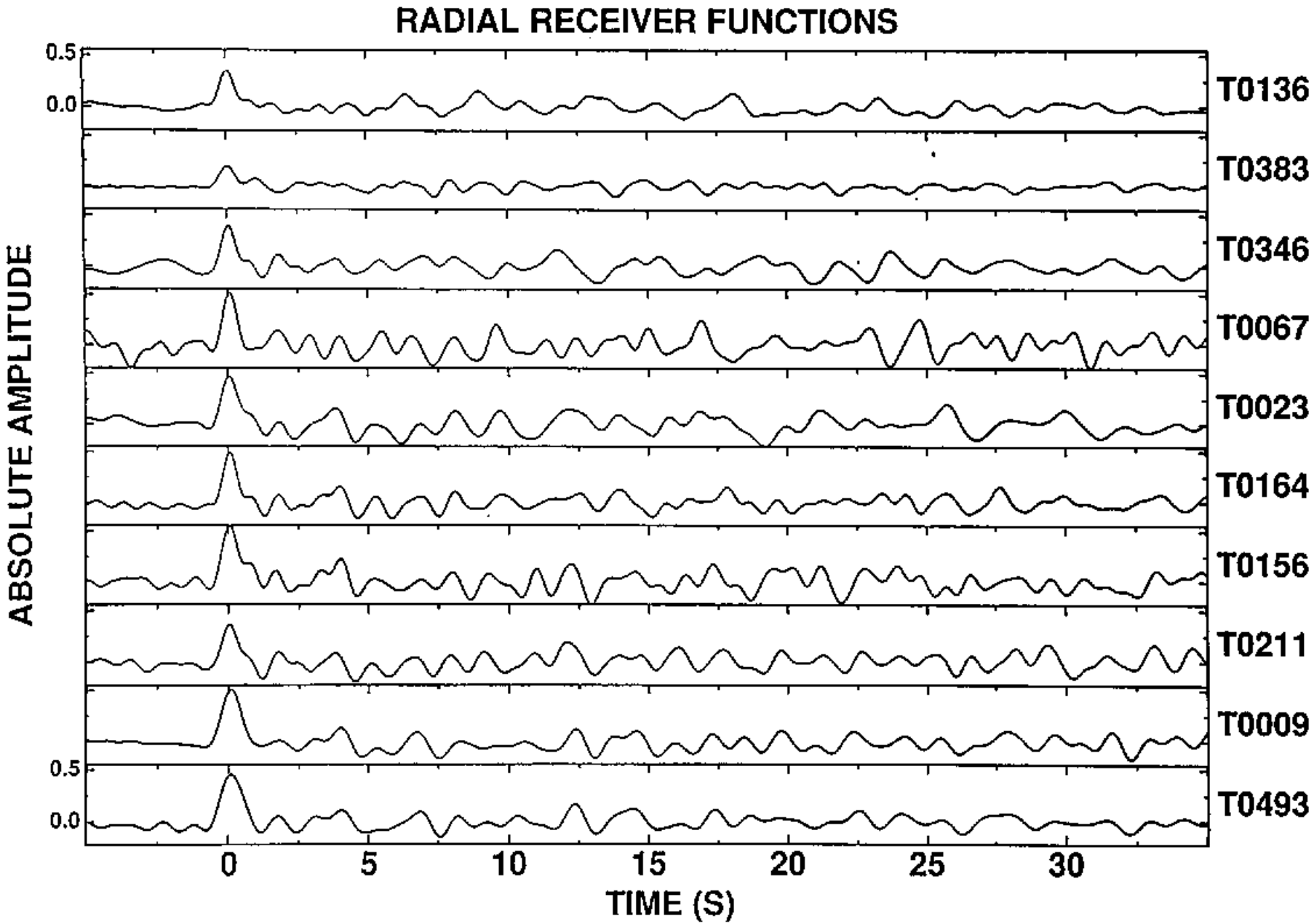
RADIAL RECEIVER FUNCTIONS
ABSOLUTE AMPLITUDE
0.5
0.0
T0136
T0383
T0346
T0067
T0023
T0164
T0156
T0211
T0009
0.5
0.0
T0493
0
5
10
15
20
25
30
TIME (S)

Figure 4

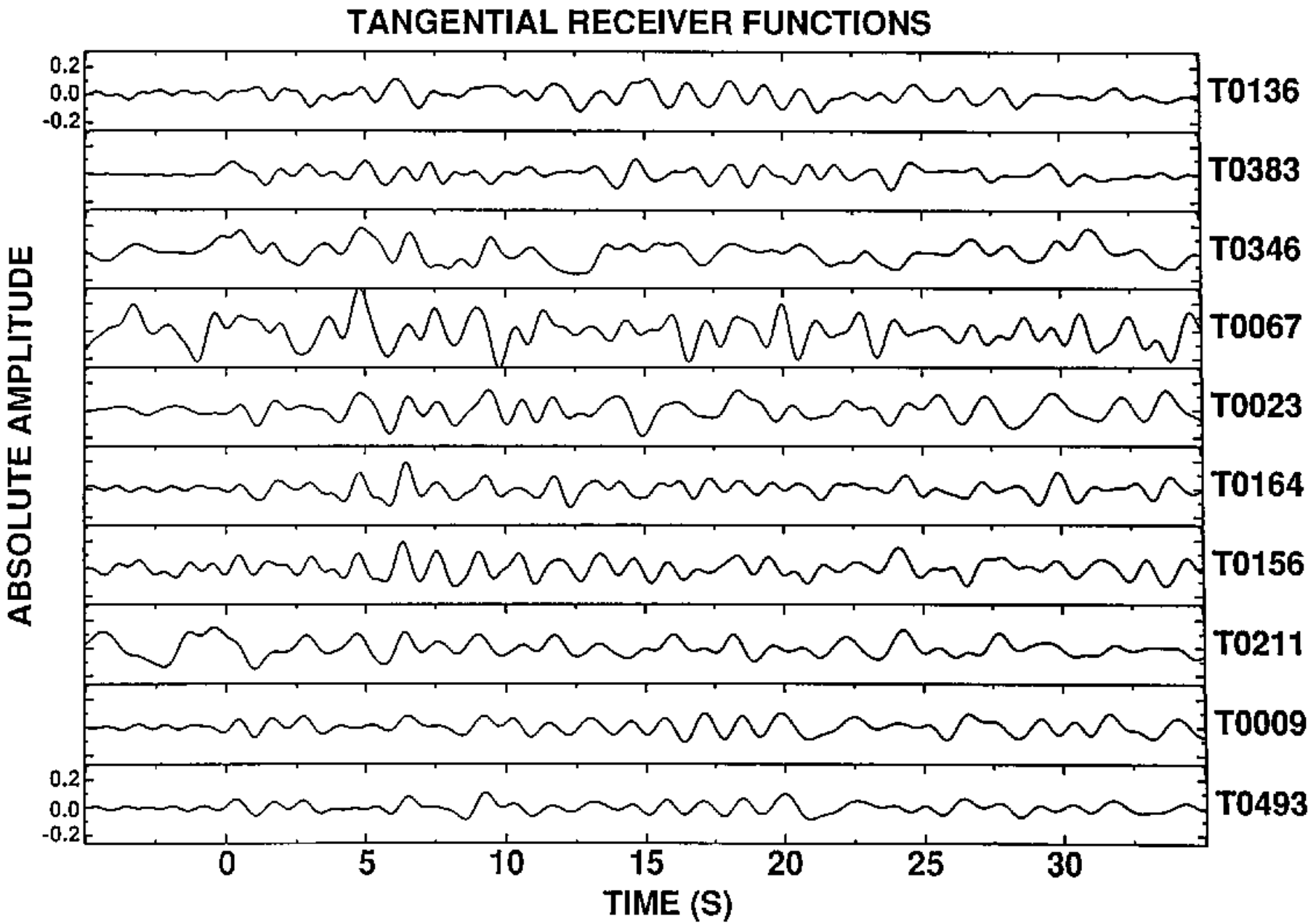
TANGENTIAL RECEIVER FUNCTIONS
ABSOLUTE AMPLITUDE
0.2
0.0
-0.2
T0136
T0383
T0346
T0067
T0023
T0164
T0156
T0211
T0009
T0493
0
5
10
15
20
25
30
TIME (S)

Figure 5

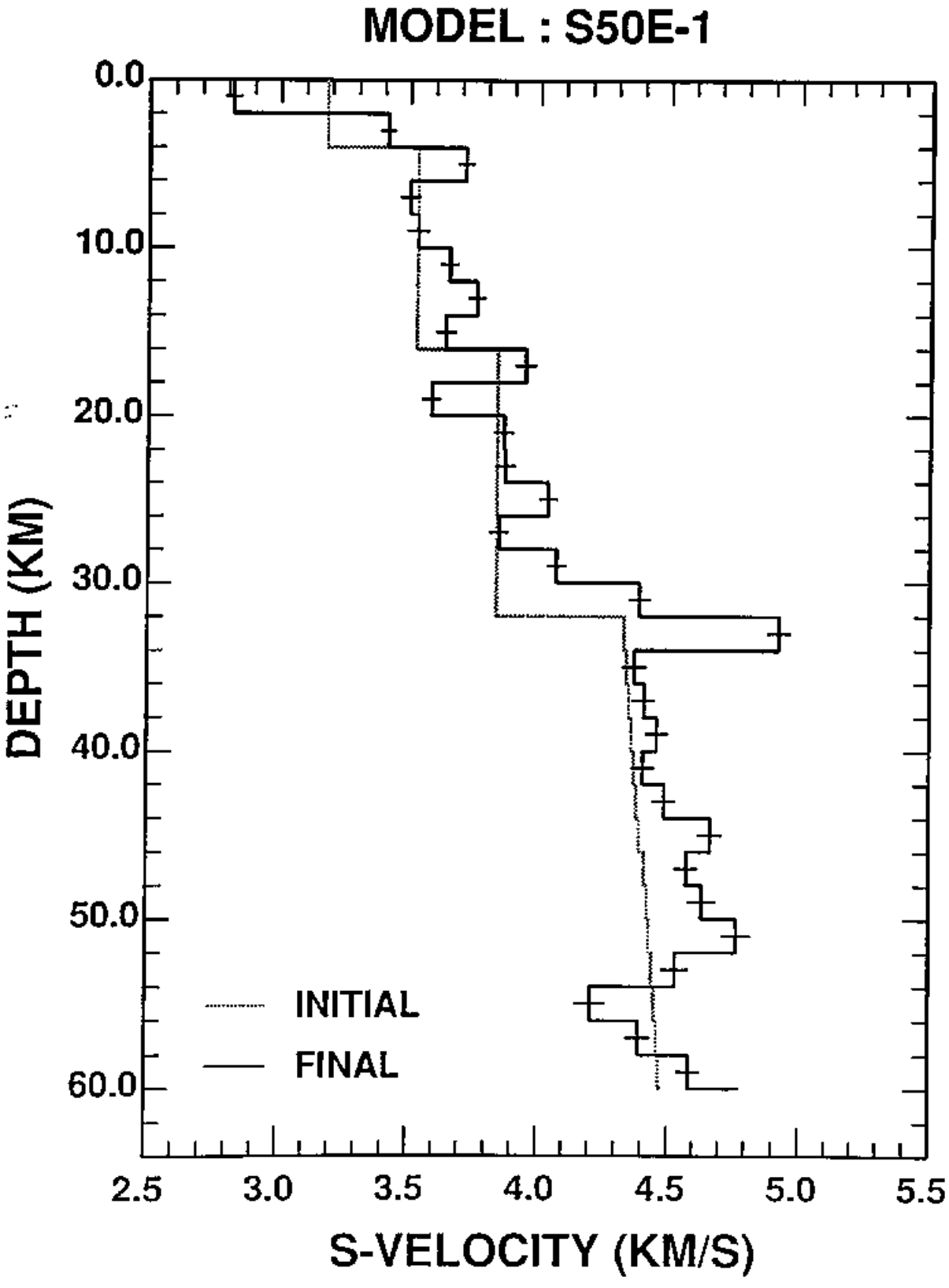
MODEL : S50E-1
0.0
10.0
20.0
30.0
40.0
50.0
60.0
DEPTH (KM)
INITIAL
FINAL
2.5
3.0
3.5
4.0
4.5
5.0
5.5
S-VELOCITY (KM/S)

Figure 6

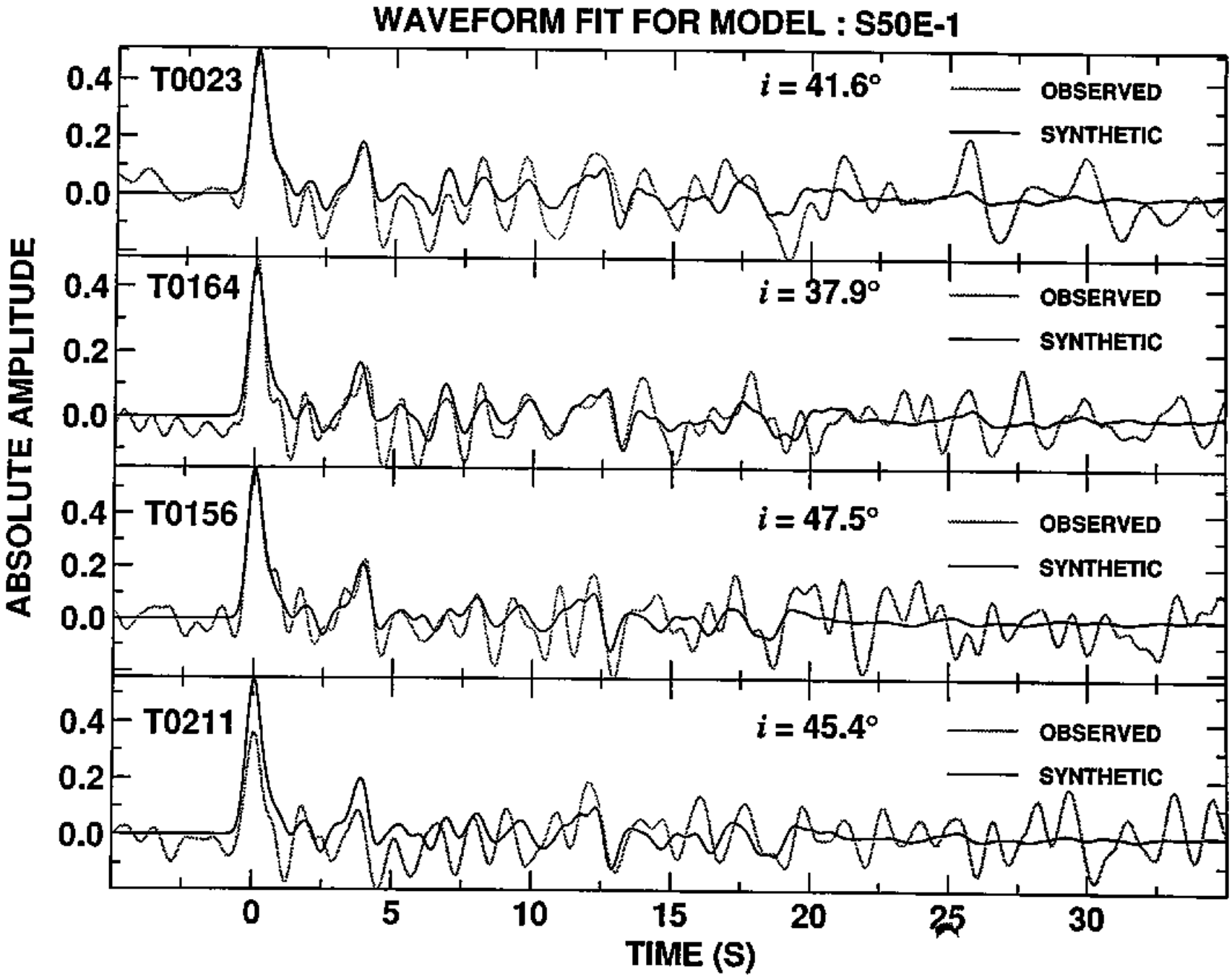
WAVEFORM FIT FOR MODEL : S50E-1
T0023
i = 41.6°
T0164
i = 37.9°
T0156
i = 47.5°
T0211
i = 45.4°
OBSERVED
SYNTHETIC
ABSOLUTE AMPLITUDE
0.4
0.2
0.0
0
5
10
15
20
25
30
TIME (S)

Figure 7

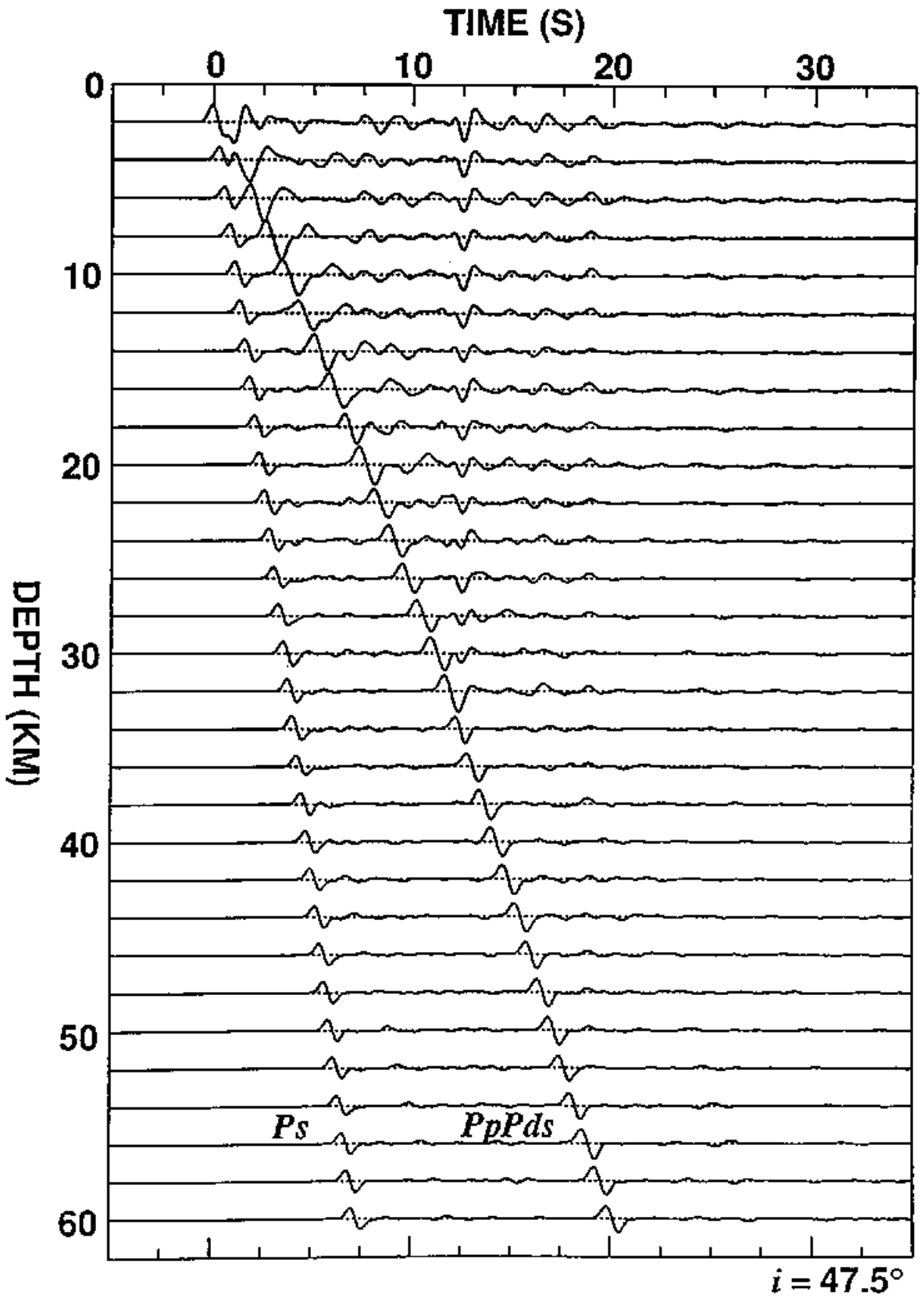
DIFFERENTIAL RADIAL RECEIVER FUNCTIONS
TIME (S)
0
10
20
30
DEPTH (KM)
0
10
20
30
40
50
60
Ps
PpPds
i = 47.5°

Figure 8

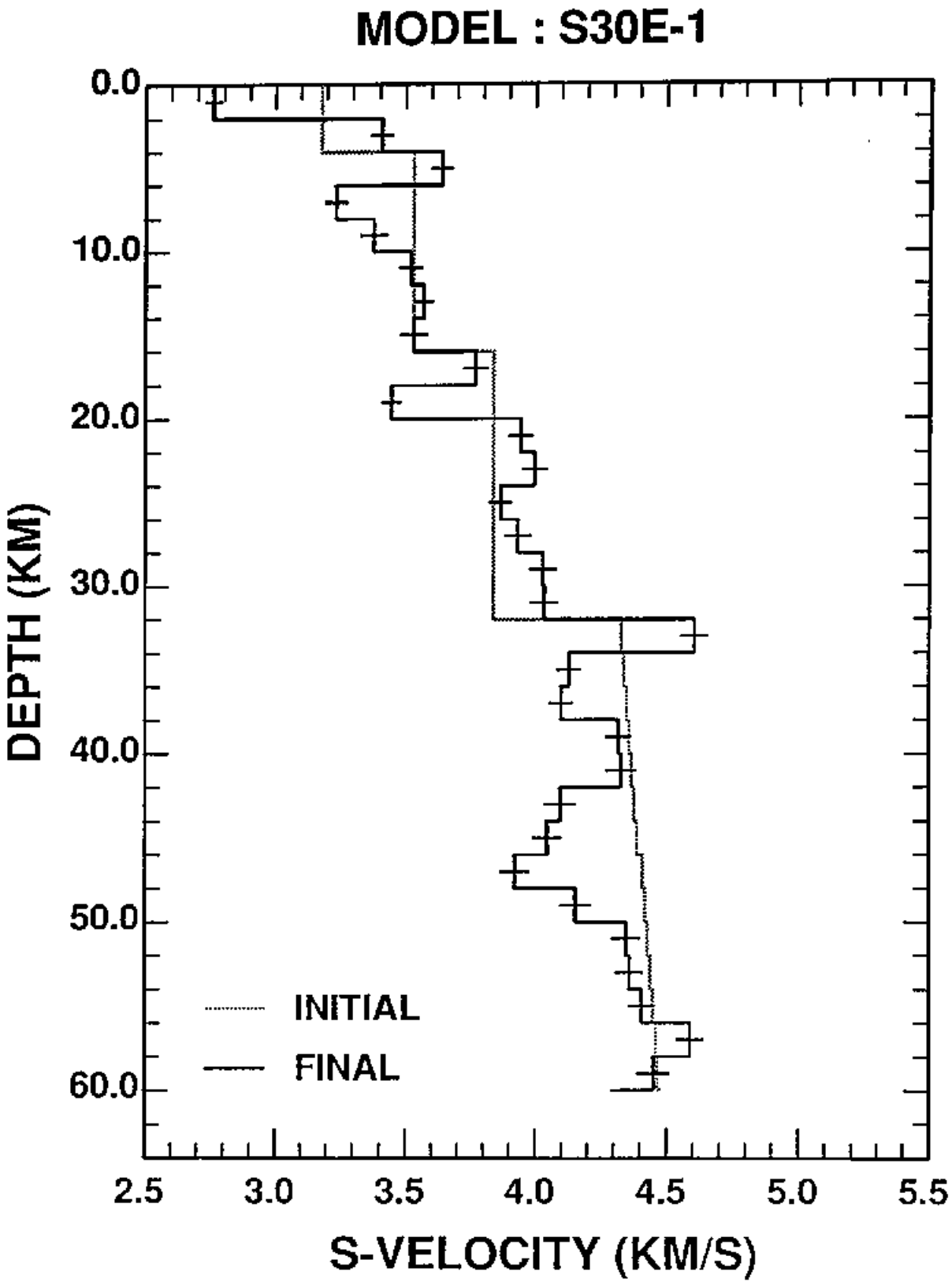
MODEL : S30E-1
0.0
10.0
20.0
30.0
40.0
50.0
60.0
DEPTH (KM)
INITIAL
FINAL
2.5
3.0
3.5
4.0
4.5
5.0
5.5
S-VELOCITY (KM/S)

Figure 9

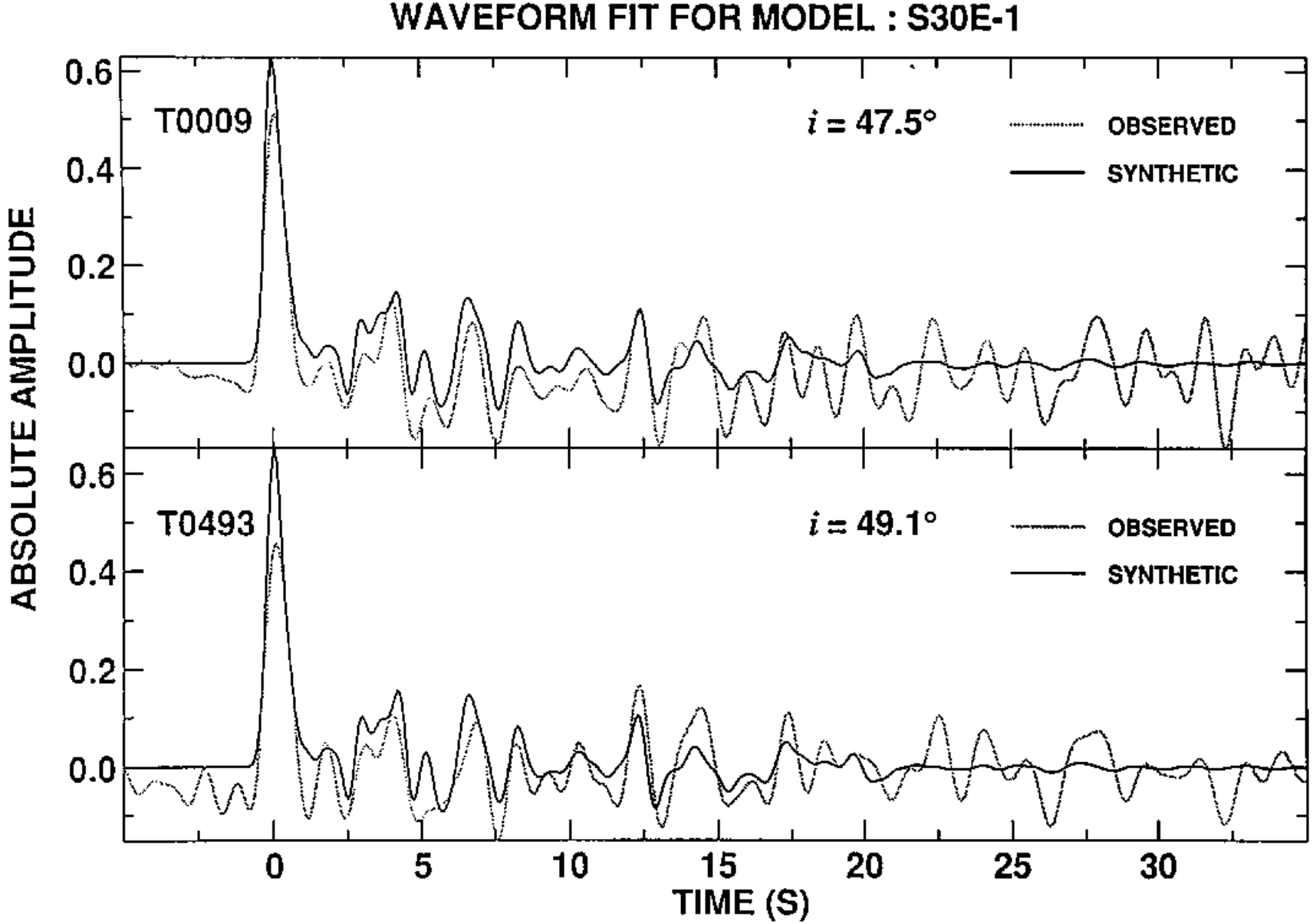
WAVEFORM FIT FOR MODEL : S30E-1
T0009
i = 47.5°
OBSERVED
SYNTHETIC
T0493
i = 49.1°
OBSERVED
SYNTHETIC
ABSOLUTE AMPLITUDE
0.6
0.4
0.2
0.0
0
5
10
15
20
25
30
TIME (S)

Figure 10

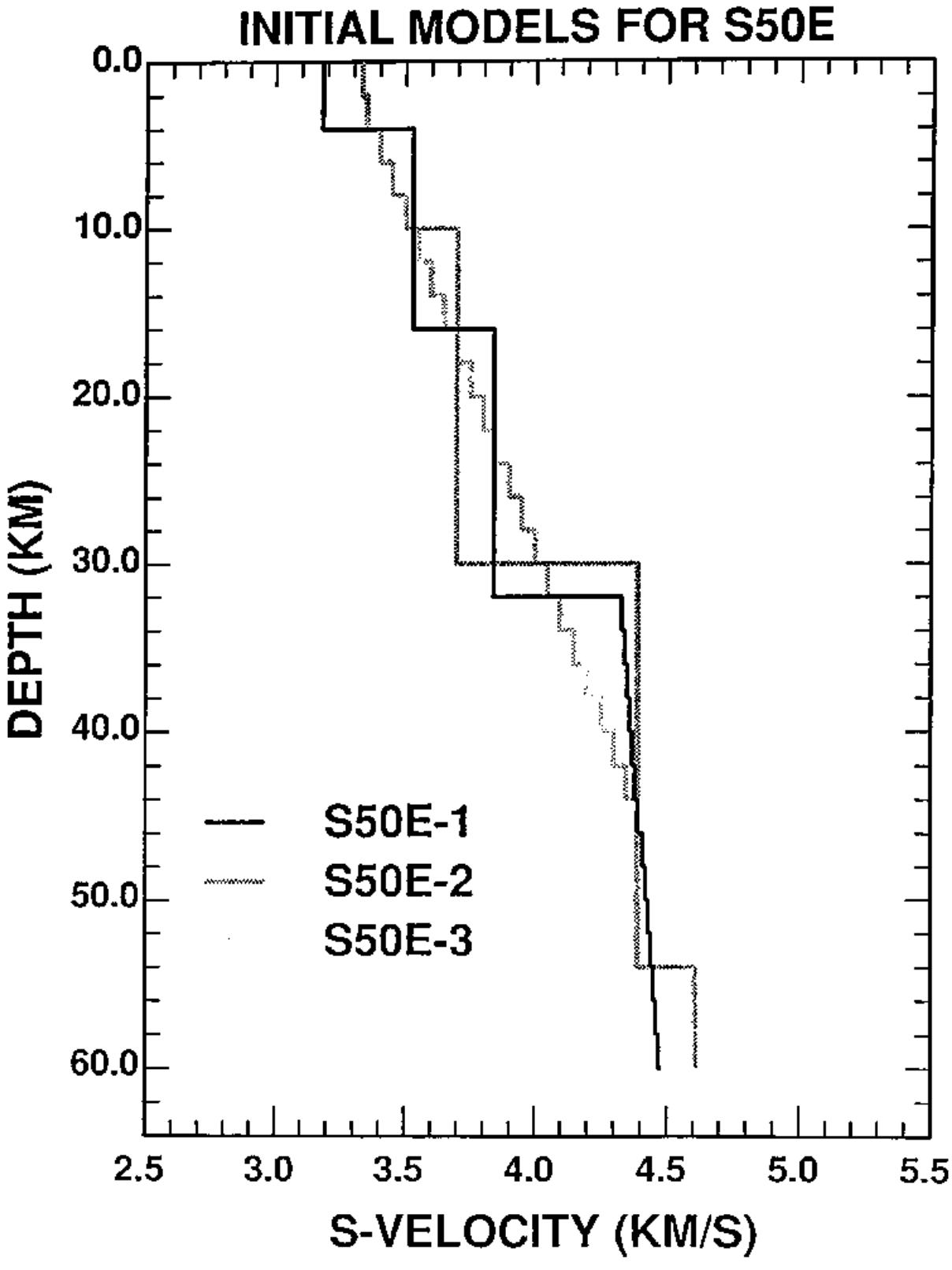
INITIAL MODELS FOR S50E
0.0
10.0
20.0
30.0
40.0
50.0
60.0
DEPTH (KM)
S50E-1
S50E-2
S50E-3
2.5
3.0
3.5
4.0
4.5
5.0
5.5
S-VELOCITY (KM/S)

Figure 1e

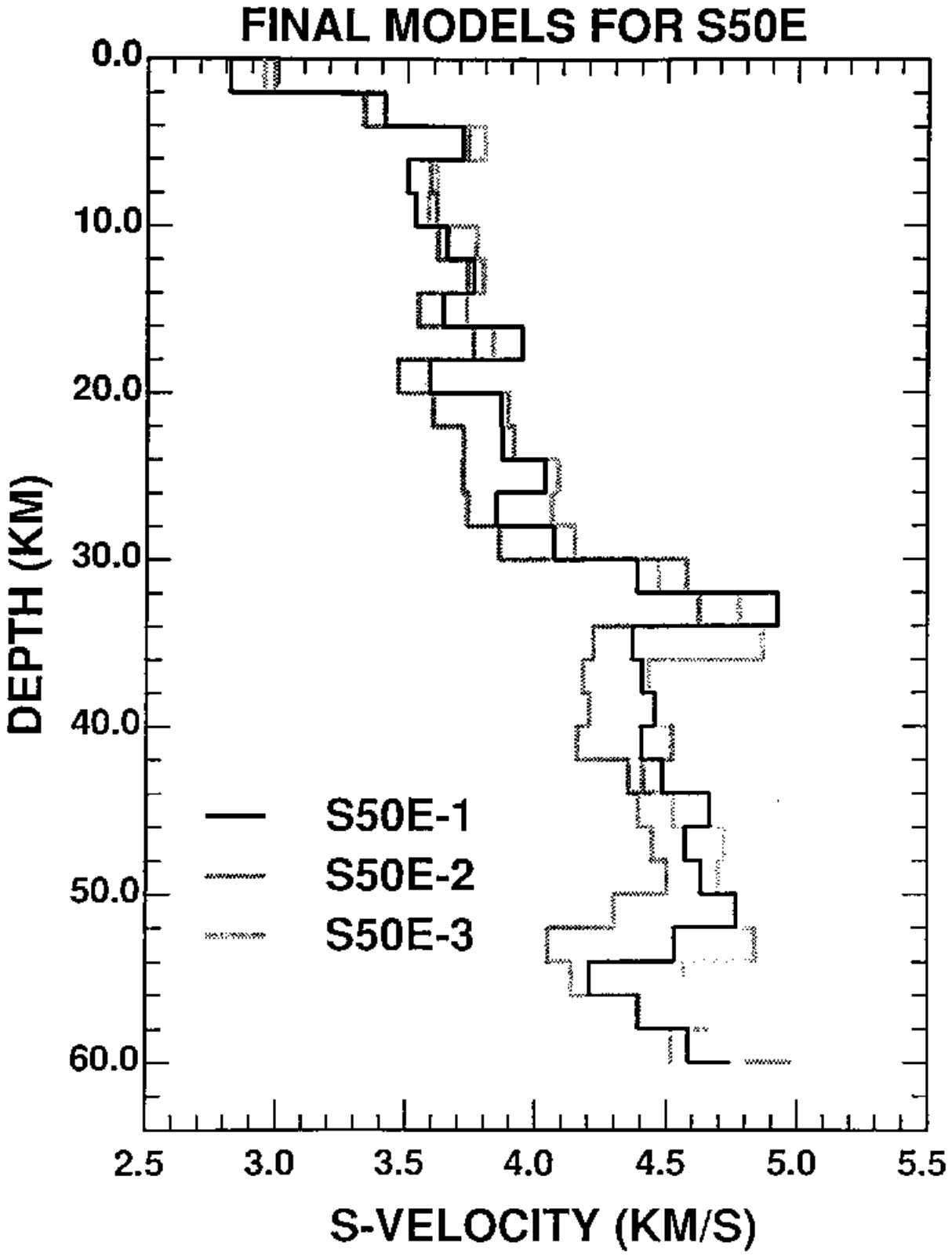
FINAL MODELS FOR S50E
0.0
10.0
20.0
30.0
40.0
50.0
60.0
DEPTH (KM)
S50E-1
S50E-2
S50E-3
2.5
3.0
3.5
4.0
4.5
5.0
5.5
S-VELOCITY (KM/S)

Figure 12

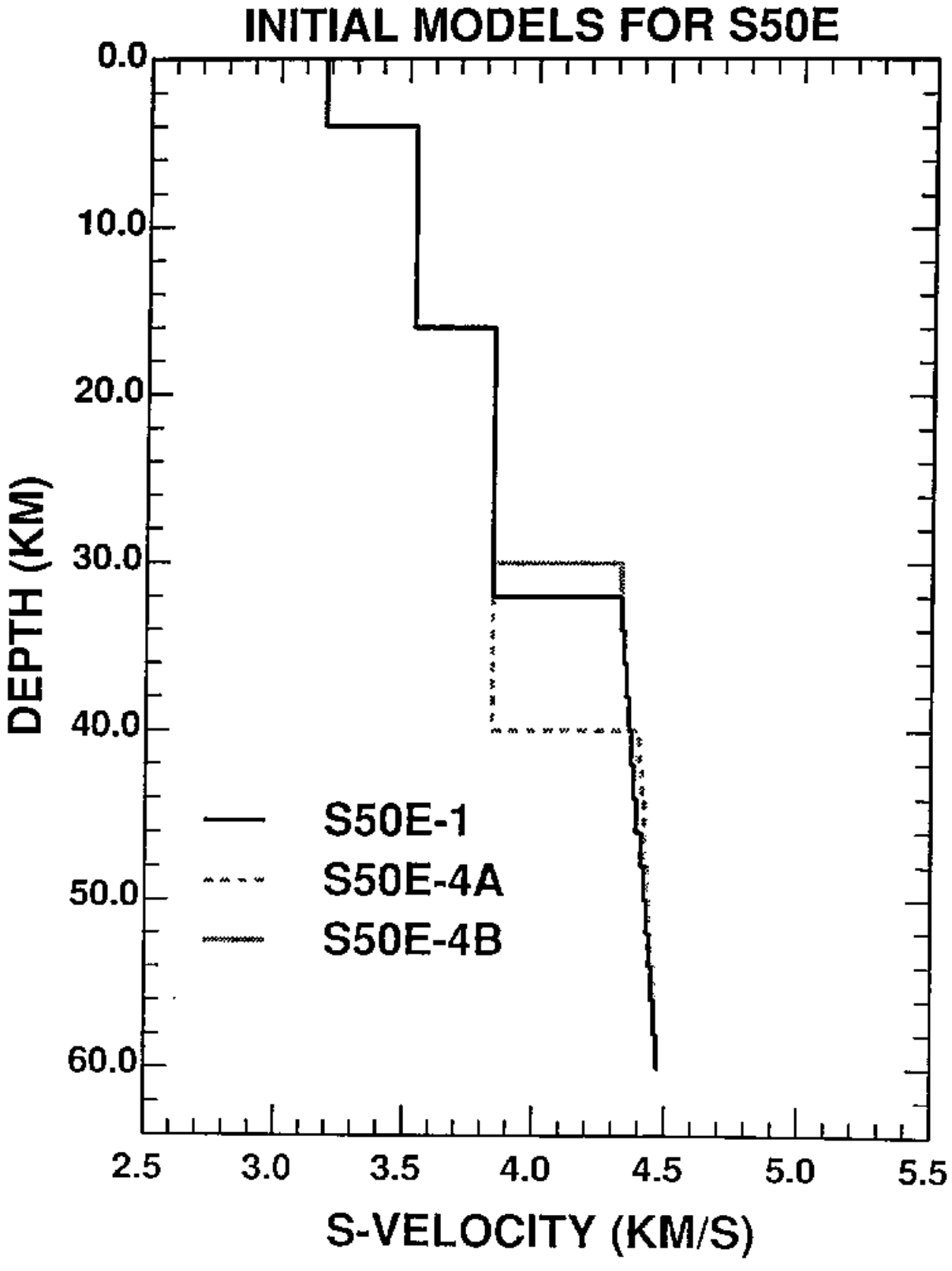
INITIAL MODELS FOR S50E
0.0
10.0
20.0
30.0
40.0
50.0
60.0
DEPTH (KM)
S50E-1
S50E-4A
S50E-4B
2.5
3.0
3.5
4.0
4.5
5.0
5.5
S-VELOCITY (KM/S)

Figure 13

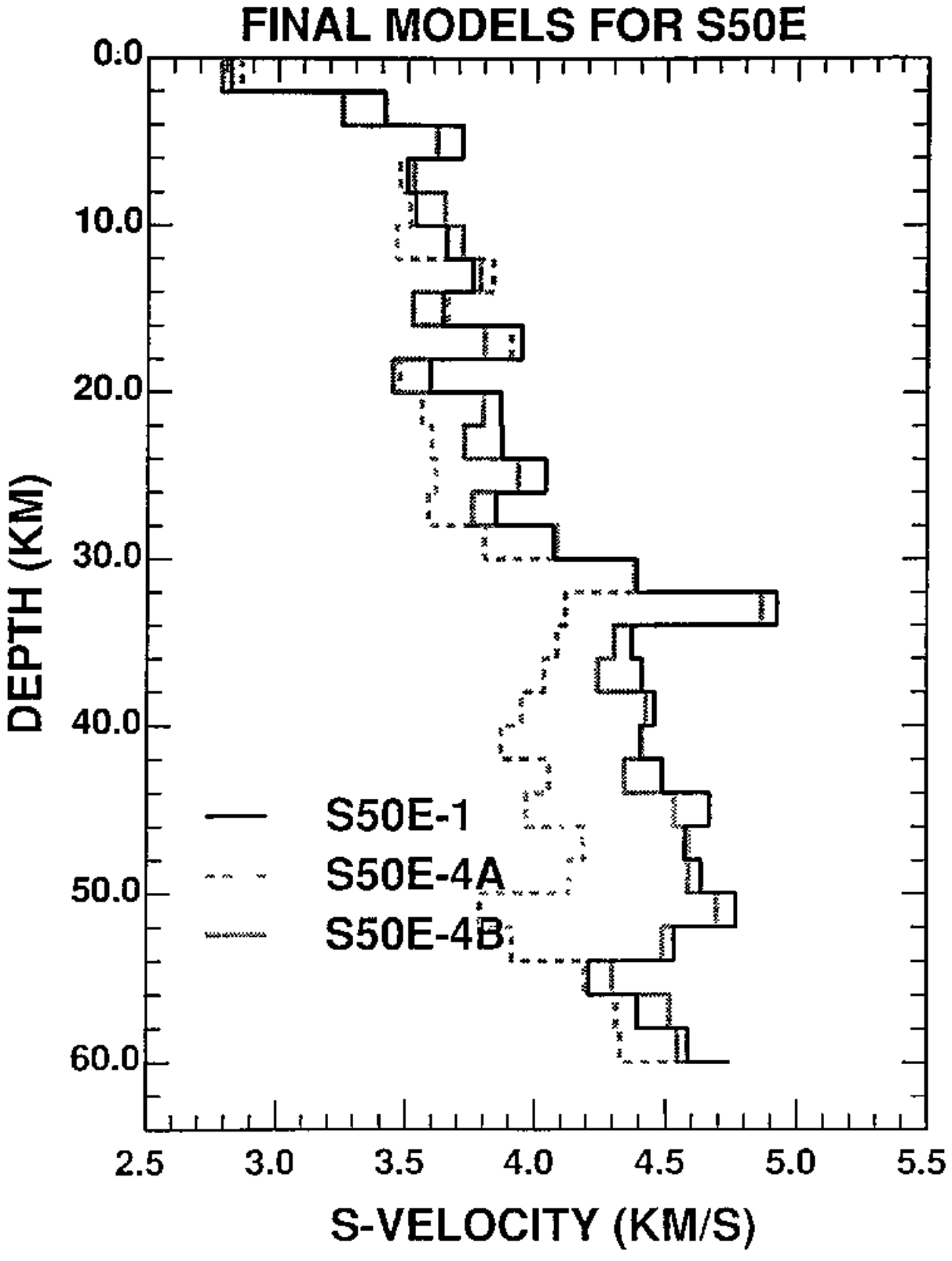
FINAL MODELS FOR S50E
0.0
10.0
20.0
30.0
40.0
50.0
60.0
DEPTH (KM)
S50E-1
S50E-4A
S50E-4B
2.5
3.0
3.5
4.0
4.5
5.0
5.5
S-VELOCITY (KM/S)

Figure 14

Numerical experiments on the multi-trace receiver function inversion to estimate S wave velocity structure of the crust and uppermost mantle

Takuo Shibutani
Research Center for Earthquake Prediction
Disaster Prevention Research Institute
Kyoto University
Uji 611, JAPAN
e-mail: shibutan@epdpri1.dpri.kyoto-u.ac.jp

Submitted to GJI on 12 Feb. 1993

Abbreviated title: The multi-trace receiver function inversion.

SUMMARY

Recently a time-domain inversion method using broadband P waveforms to obtain a 1-D fine-scale S wave velocity structure of the lithosphere, what is called a receiver function inversion, was developed and applied to various kinds of tectonic regions. Since the receiver function inversion assume a horizontally layered model, we can not use receiver functions that are strongly infected by background noises, scattered waves due to small scale heterogeneities and converted waves at dipping interfaces. We must know the allowable upper limit of the noise level.

In this paper we estimate the maximum allowable noise level by numerical experiments, and frequency range of receiver functions we can use by spectrum analysis. For both regional receiver functions derived from nearby deep events and teleseismic receiver functions, the available frequency range is lower than 0.5 Hz, because in the higher frequencies, especially higher than 1.0 Hz, the scattered waves contaminate significantly the receiver functions.

Since all tangential energy of a P waveform is from the noises, we can estimate the noise level by an rms amplitude ratio between the tangential and the radial component. From results of the numerical experiments the allowable upper limit of the noise level is estimated at 0.6 in the rms amplitude ratio for typical regional receiver functions.

Finally we propose an effective approach of the receiver function inversion.

Key words: receiver function, multi-trace inversion, numerical experiment

1 INTRODUCTION

Owens, Zandt and Taylor (1984) developed a time-domain inversion method using teleseismic P waveforms to obtain a 1-D detailed S wave velocity structure down to the uppermost mantle, which was called a receiver function inversion. The receiver functions are derived from broadband teleseismic P waveforms by using the source equalization procedure of Langston (1979). The radial component is comprised by P-to-S converted waves at discontinuities in the earth's interior. And a stacked radial receiver function is inverted for a 1-D S wave velocity model. There have been many studies using this methods, for example, Owens, Taylor and Zandt (1987), Owens, Crosson and Hendrickson (1988), Lapp, Crosson and Owens (1990), Cassidy and Ellis (1991) and so forth.

Recently we applied this method to a site in Honshu, Japan (Shibutani 1993). Instead of teleseismic receiver functions, we used regional receiver functions which were derived from P waveforms of nearby deep earthquakes. Furthermore we developed a new method of multi-trace inversion in which several receiver functions are inverted simultaneously for one velocity model. The receiver functions can be formed from P waves with different incident angles.

Since the regional receiver functions are derived from P waveforms of nearby deep earthquakes, they are expected to have more short period energy than the teleseismic receiver functions. This suggests that the inversion using the regional receiver functions has possibility of obtaining a finer-scale model than the teleseismic receiver function inversion. However the short period signals are often contaminated by scattered waves due to small scale heterogeneities. If the signal-to-noise ratio is poor, we would be misled to a overly complicated model, because the noises are interpreted as P-to-S converted waves at discontinuities in the model. In this paper we examine this feature in detail, give the upper limit of frequencies that we can use in the regional receiver functions and compare it with that of the teleseismic receiver functions.

There seems to be implicit understanding that the best approach of the radial receiver function inversion is to invert only for S wave velocity, adjusting P wave velocity and density appropriately. We check the possibility whether the P wave velocity and the density can be determined without dependence on the S wave velocity by using differential radial receiver functions.

We indicated in the paper (Shibutani 1993) that the radial receiver functions with close backazimuths have very similar waveforms, but those with distant backazimuths of greater than 10° do not, and that some of the tangential receiver functions have considerably large energy although they are less correlated with each other. This suggests that there are lateral heterogeneities beneath the stations but the structure does not change so much in the azimuth range of 10°, and that there are small scale heterogeneities that generate scattered waves. In the cases where the energy ratio of a tangential component to a radial component is large, the radial receiver functions are thought to be contaminated by the scattered waves as well as the tangential receiver functions and, therefore, they would mislead us to a wrong final model. We investigate the effect of random noises on final models by numerical experiments and estimate the allowable upper limit of the noise level of the receiver functions.

2 FREQUENCY UPPER LIMIT OF RECEIVER FUNCTIONS

Table 1: Location of nearby deep events

Table 2: Location of teleseismic events

The regional receiver functions derived from P waveforms of nearby deep earthquake contain high frequency waves more than the teleseismic receiver functions. Therefore, it seems that the inversion using the regional receiver functions can obtain

finer-scale velocity models than the teleseismic receiver function inversion. However, the high frequency waves are often infected by background noises and signal generating noises such as scattered waves due to small scale heterogeneities more intensely than the lower frequency waves. Thus we must be careful in using high frequency receiver functions, unless we would obtain overly complicated models, because the noises are interpreted as P-to-S converted waves at discontinuities in the 1-D models. So in order to estimate the upper limit of frequencies that can be used in the receiver functions, we investigate the frequency content of the P waveforms of both nearby deep events and teleseismic events.

Figure 1: Amplitude spectra for nearby deep events

Fig. 1 shows amplitude spectra of P waveforms of nearby deep events which are listed in Table 1. In the cases of T0136, T0383, T0164, T0156, T0009 and T0493, the S/N ratios of the vertical and the radial component are enough high in the whole frequency range, so that the background noises do not infect the receiver functions significantly. However, in the cases of T0346, T0067, T0023 and T0211, the S/N ratios around frequencies of $0.2 \sim 0.3$ Hz are poor, therefore we should prevent from using these frequencies if they seriously infect the receiver functions. The fact that even the tangential component has a high S/N ratio implies that some energy of P waves leaks to the tangential component by scattering at small scale heterogeneities and/or by converting at dipping interfaces. The level of the amplitude spectrum of the tangential component is lower than that of the other components in the frequencies lower than $0.5 \sim 0.6$ Hz, but the levels are comparable in the higher frequencies. Consequently the radial receiver functions might be contaminated by the signal generating noises in the frequencies higher than 0.6 Hz. So we should use waves whose frequency are lower than 0.5 Hz for the regional receiver functions.

Fig. 2 shows amplitude spectra of P waveforms of teleseismic events which are listed in Table 2. In the cases of the events of T0038 and T0138, the S/N ratios of all three components are poor in the frequencies greater than $0.3 \sim 0.5$ Hz, which

suggests that background noises contaminate the receiver functions significantly. In the other cases the S/N ratios are good but the level of the amplitude spectrum of the tangential P waveforms is comparable with that of the other components in the frequencies greater than 0.5 Hz. Since the receiver functions are thought to be polluted by the scattered noises in these frequencies, we should restrict to using waves whose frequency are lower than 0.5 Hz.

Figure 2: Amplitude spectra for teleseismic events

Consequently, for the site studied in the paper (Shibutani 1993), upper limit of frequencies we can use in the receiver functions is 0.5 Hz in both cases of nearby deep invents and teleseismic events. Therefore it is impossible to obtain a finer-scale model by using the regional receiver functions than the teleseismic receiver functions. However there is an advantage in the amplitude of the P-to-S converted waves in the case of the regional receiver functions against the teleseismic receiver functions. This will be discussed later in relation to the numerical experiments.

3 MODEL PARAMETERS OF RADIAL RECEIVER FUNCTION INVERSION

Owens et al. (1984) said that the best approach of receiver function inversion is to invert only for S wave velocity, adjusting P wave velocity and density appropriately. Succeeding studies followed in the step of them and restricted the model parameter of the inversion to the S wave velocity. However, is there any possibility whether the P wave velocity and the density can be determined without dependence on the S wave velocity? We check this by comparing differential radial receiver functions due to the three possible parameters' perturbation.

We can calculate response of a 1-D model by using a Thomson-Haskell matrix method (Haskell 1962) and obtain a synthetic radial receiver function by deconvolving a vertical component from a radial component. Then the synthetic radial

receiver function is considered to be a function of the density, P wave velocity and S wave velocity in each layer and expressed by

$$R_i(\rho, \alpha, \beta) ,$$

where suffix i denotes time sampling point, $\rho = (\rho_1, \rho_2, \cdots, \rho_M)$ is the density, $\alpha = (\alpha_1, \alpha_2, \cdots, \alpha_M)$ is the P wave velocity, $\beta = (\beta_1, \beta_2, \cdots, \beta_M)$ is the S wave velocity and suffix M denotes the number of layers in the model.

Figure 3: Velocity model and ray diagram

Figure 4: Differential radial receiver function due to S wave velocity perturbation

For example, differential radial receiver function generated by perturbation of the S wave velocity in k-th layer is represented by

$$\frac{\partial R_i(\rho, \alpha, \beta)}{\partial \beta_k} = \frac{R_i(\rho, \alpha, \beta_1, \cdots, \beta_k + \Delta\beta_k, \cdots, \beta_M) - R_i(\rho, \alpha, \beta_1, \cdots, \beta_k, \cdots, \beta_M)}{\Delta\beta_k} ,$$

where $k = 1, 2, \cdots, M$. Therefore the differential radial receiver function shows what effects would be caused on the radial receiver function if the S wave velocity in the k-th layer is perturbed.

Fig. 4 shows the differential radial receiver functions due to S wave velocity perturbation for a velocity model illustrated in Fig. 3. The velocity model has 30 layers and the thickness of each layer is 2 km. We can find that P-to-S converted waves Ps and $PpPds$ have almost the same amplitude at all depths. This suggests that the S wave velocity in each layer can be determined with the same resolution. Further at depths above the pre-existing discontinuities such as the Moho, there are characteristic phases of the discontinuities. These phases can contribute to determining the depth of the discontinuities.

Figure 5: Differential radial receiver function due to density perturbation

Fig. 5 shows differential radial receiver functions due to density perturbation. The P-to-S converted waves $PpPds$ and $PpSds$ are clear but there is no Ps phase. And the amplitudes of these differential radial receiver functions are a little smaller than that of those due to the S wave velocity perturbation.

Figure 6: Differential radial receiver function due to P wave velocity perturbation

Fig. 6 shows differential radial receiver functions due to P wave velocity perturbation. They are comprised mainly by the characteristic phases of the pre-existing discontinuities and their amplitudes are smaller than one-tenth of the other types of differential radial receiver functions Therefore the P wave velocity can not be well constrained by the radial receiver function inversion.

Figure 7: Differential radial receiver function due to S wave velocity perturbation with P wave velocity and density adjusted appropriately

We can conclude from these results that the best approach of the radial receiver function inversion is to restrict the model parameter to only S wavevelocity with P wave velocity and density adjusted by using appropriate relationships as pointed out by Owens et al. (1984). Fig. 7 shows differential radial receiver functions due to S wave velocity perturbations. But in this case P wave velocity and density are adjusted by following relationships;

$$\alpha = \begin{cases} 1.73\,\beta, & \text{for the crust} \\ 1.80\,\beta, & \text{for the mantle} \end{cases} \tag{1}$$

$$\rho = 2.35 + 0.036(\alpha - 3.0)^2. \tag{2}$$

This figure shows that the major P-to-S converted waves Ps, $PpPds$ and $PpSds$

4 EFFECTS OF RANDOM NOISES ON FINAL MODELS

The real structure of the earth's interior has various kinds of heterogeneities that generate scattered waves. However, our model in the radial receiver function inver-

sion is vertically one-dimensional, so the scattered waves behave as noises in our inversion. Since all tangential energy of P waveforms is generated by the scattered waves and background noises, we can estimate how the P waveforms are infected by these noises by comparing energy between the tangential component and the other two components. If the energy ratio of the tangential component to the radial component is high, the radial receiver function would be seriously infected by the noises and such receiver functions would mislead us to a wrong final model. Thus we must know the allowable upper limit of the noise level of the receiver functions. In order to estimate the limit, we investigate the effects of the random noises on final models by numerical experiments.

First we calculate synthetic waveforms for a model illustrated in Figs. 8, 10 and 12 as a true model. Secondly we add random noises to the synthetic waveforms and calculate radial receiver functions by deconvolving the vertical component from the radial component of the synthetic waveforms. Thirdly the radial receiver functions are inverted with an initial model illustrated in the figures. We made three experiments with changing the noise level and the method of the inversion.

4.1 Experiment 1

Figure 8: True, initial and final models for experiment 1

Figure 9: Waveform fit for experiment 1

In the first experiment we calculated three components of synthetic waveforms for three incident angles of 30°, 35° and 40° and add different random noises to each traces. The amplitude of the noises is adjusted to be roughly equal to that of the $PpPms$ phases (m denotes the Moho) in the radial component. In this case the ratios of rms amplitude between the tangential and the radial receiver functions are $0.1 \sim 0.2$, which are a little smaller than in real cases studied in the paper (Shibutani 1993). These three pseudo-observed radial receiver functions are inverted

by the multi-trace inversion developed in the above paper. The result is shown in Fig. 8. The final model is in good agreement with the true model. The waveform fit between the pseudo-observed and synthetic receiver functions is shown in Fig. 9. The major converted phases are well fitted.

4.2 Experiment 2

Figure 10: True, initial and final models for experiment 2

Figure 11: Waveform fit for experiment 2

In the second experiment we calculate three sets of three component synthetic waveforms for an incident angle of 40° and add different random noises to each traces. The amplitude of the noises is the same as in the first experiment. Then three radial receiver functions derived from the three sets of the synthetic waveforms are stacked to enhance common phases. The stacked radial receiver function is inverted. The result is shown in Fig. 10. The coincidence between the final model and the true model is good on the whole, but not so good as in the first experiment. The waveform fit for this case is shown in Fig. 11. The major converted phases are also well fitted as in the case of the first experiment.

Comparison of the results between the first and the second experiment shows that the multi-trace inversion has a advantage against the single-trace inversion using a stacked receiver function. In the multi-trace inversion we can use several receiver functions with different incident angles. Since the relative travel times between the P-to-S converted phases and the direct P waves are different among the receiver functions, the multi-trace receiver function can utilize more information than the single-trace inversion. Therefore the multi-trace inversion can obtain better model than the single-trace inversion.

4.3 Experiment 3

The third experiment is the same as the first experiment except that the amplitude of the added random noises is larger, that is, roughly equal to that of the Ps phases at the Moho. In this case the ratios of the rms amplitude between the tangential and the radial receiver function are $0.6 \sim 0.7$, which are a little larger than in the real cases studied in the previous paper. The resulting final model is shown in Fig. 12 and the waveform fit between the pseudo-observed and synthetic receiver functions is shown in Fig. 13. The agreement between the final model and the true model is considerably good at depths shallower than 22 km, while in the deeper region it is not so good. The velocity jump at the Moho discontinuity in the final model is about half of that in the true model. However, considering that the added random noises have the same amplitude as the largest converted phases, the coincidence between the final and the true model seems to be rather good.

Figure 12: True, initial and final models for experiment 3

Figure 13: Waveform fit for experiment 3

We conclude from these results that the allowable upper limit of the noise level of receiver functions is 0.6 in the rms amplitude ratio between the tangential and the radial component.

Figure 14: Amplitude vs. incident angle

Fig. 14 shows the relation between the amplitude of the major phases in radial receiver functions and the incident angles of the P waves at the bottom of the modeled layers. The incident angles vary from 35° to 50° for the nearby deep events which we used in the paper (Shibutani 1993), while they vary from 25° to 40° for teleseismic events whose epicentral distances are $35° \sim 70°$. Therefore this figure indicates that Ps phases of the regional receiver functions are larger than those

of the teleseismic receiver functions, that *PpPms* phases have the same amplitude between the two receiver functions and that *PpSms* phases of the regional receiver functions are smaller than those of the teleseismic receiver functions. However the *PpSms* phases are not so significant as the other two phases because the former are much smaller than the latter. In the above experiments we showed that the noise level in the radial receiver functions must be smaller than the *Ps* phases and that the smaller the noise level is, the more reliable model we can obtain. Thus in a case where the noise level is the same between the regional and the teleseismic receiver functions, the inversion using the regional receiver functions can obtain more reliable model than those using the teleseismic receiver functions because the *Ps* phases in the former are larger than those in the latter.

5 CONCLUSIONS

This paper contains three subjects. First we estimated the upper limit of frequencies that we can use in the radial receiver function inversion by investigating amplitude spectra of three components of *P* waveforms. The level of the amplitude spectrum of the tangential component is comparable with that of the other components in the frequencies higher than 0.5 Hz in the cases of both nearby deep events and teleseismic events. This means that scattered waves are dominant and the radial receiver function might be infected by the noises in these frequencies. Therefore the upper limit is considered to be 0.5 Hz for our studying site in Honshu, Japan.

Secondly we investigated a possibility whether *P* wave velocity and density can be determined without dependence on *S* wave velocity by comparing differential radial receiver functions due to the three possible parameters' perturbation. The results indicate that the radial receiver functions are most sensitive to the *S* wave velocity, the second is the density and the most insensitive parameter is the *P* wave velocity. Therefore the best approach of the radial receiver function inversion is to invert only for the *S* wave velocity, adjusting the density and the *P* wave velocity

appropriately just as pointed out by Owens et al. (1984).

Thirdly we investigated effects of random noises on final models in order to estimate the allowable upper limit of the noise level of the receiver functions. Since all tangential energy of P waveforms are generated by scattered waves due to small scale heterogeneities and background noises, we can estimate the noise level of the radial receiver functions by a ratio of rms amplitude between the tangential and the radial component. Comparing the result of the first experiment in the section 4 with that of the third experiment, the allowable upper limit of the noise level is estimated to be 0.6 in the ratio of the rms amplitude.

Comparison of the results between the first and the second experiment shows us an advantage of the multi-trace inversion against the single-trace inversion. The final model of the former is better than that of the latter. The multi-trace inversion can invert several receiver functions that have different incident angles. And the relative travel times between P-to-S converted phases and the direct P phases are different among the receiver functions, therefore the multi-trace inversion can utilize more information than the single-trace inversion. This is the reason why the multi-trace inversion has the advantage against the single-trace inversion.

Finally we propose an effective approach of the radial receiver function inversion.

1. We check amplitude spectra of three components of P waveforms we analyze. We choose the P waveforms having high signal-to-noise ratio through frequency range of $0.1 \sim 1.0$ Hz. Since tangential component is generated by mainly scattered waves due to small scale heterogeneities, we can not use frequency range in which the level of the amplitude spectrum of the tangential component is comparable with that of the other two components. So we must eliminate waves having these frequencies from the original P waveforms by high-cut filtering.

2. We choose radial receiver functions which have similar waveforms, especially

for P-to-S converted waves such as Ps, $PpPds$ and $PpSds$. According to our experience and a study by Flatté and Wu (1988), the radial receiver functions within the range of 10° in both backazimuth and incident angle have similar waveforms.

3. We select receiver functions whose ratio of rms amplitude between tangential and radial component is less than 0.6. If we use receiver functions with the ratio greater than this value, we would be misled to a wrong final model, because the receiver functions might be seriously infected by noises such as scattered waves and background noises and these noises would be interpreted as P-to-S converted waves at discontinuities in the model.

4. The radial receiver functions are inverted only for S wave velocity, adjusting P wave velocity and density appropriately, for a horizontally layered model of fixed thicknesses. The thicknesses are determined by considering a necessary condition between wave length (λ) and the thickness (δ); $\delta > \lambda/4$.

ACKNOWLEDGMENTS

I thank Dr. Kazuro Hirahara. I could make many fruitful discussions with him on the data processing and the inversion method. I thank Prof. Kazuo Oike and Prof. Masataka Ando for their advice and encouragement. Prof. Oike gave me a hint of the numerical experiments. Calculations were carried out at the Data Processing Center, Kyoto University.

REFERENCES

Cassidy, J. F. & Ellis, R. M., 1991. Shear wave constraints on a deep crustal reflective zone beneath Vancouver Island, J. Geophys. Res., **96**, 19,843–19,851.

Flatté, S. M. & Wu, R. S., 1988. Small-scale structure in the lithosphere and asthenosphere deduced from arrival time and amplitude fluctuations at NORSAR, J. Geophys. Res., **93**, 6601–6614.

Haskell, N. A., 1962. Crustal reflection of plane *P* and *SV* waves, J. Geophys. Res., **67**, 4751–4767.

Langston, C. A., 1979. Structure under Mount Rainier, Washington, inferred from teleseismic body waves, J. Geophys. Res., **84**, 4,749–4,762.

Lapp, D. B., Crosson, R. S. & Owens, T. J., 1990. Scattering of teleseismic body waves along the Hayward-Calaveras fault system, Bull. Seism. Soc. Am., **81**, 576–591.

Owens, T. J., Zandt, G. & Taylor, S.R., 1984. Seismic evidence for an ancient rift beneath the Cumberland Plateau, Tennessee: A detailed analysis of broadband teleseismic *P* waveforms, J. Geophys. Res., **89**, 7783–7795.

Owens, T. J., Taylor, S. R. & Zandt, G., 1987. Crustal structure at regional seismic test network stations determined from inversion of broadband teleseismic *P* waveforms, Bull. Seism. Soc. Am., **77**, 631–662.

Owens, T. J., Crosson, R. S. & Hendrickson, M. A., 1988. Constraints on the subduction geometry beneath western Washington from broadband teleseismic waveform modeling, Bull. Seism. Soc. Am., **78**, 1,319–1,334.

Shibutani, T., 1993. Multi-trace receiver function inversion of nearby deep earthquake waveforms, submitted to Geophys. J. Int.

Figure Captions

Figure 1 Amplitude spectra of 10 nearby deep events which are listed in Table 1. The event number is shown at upper-left corner in each diagram. The upper three traces are amplitude spectra for a signal time window, that is during 35 s after the direct P phase, and the lower three are for a noise time window, that is during 35 s before the P phase. Solid, dash and dotted lines denote vertical, radial and tangential component, respectively.

Figure 2 Amplitude spectra of 5 teleseismic events which are listed in Table 2. The event number is shown at upper-left corner in each diagram. The upper three traces are amplitude spectra for a signal time window, that is during 35 s after the direct P phase, and the lower three are for a noise time window, that is during 35 s before the P phase. Solid, dash and dotted lines denote vertical, radial and tangential component, respectively.

Figure 3 Four-layer-model for which synthetic radial receiver functions and differential receiver functions are calculated. Simplified rays of the major P-to-S converted waves at the Moho discontinuity are also illustrated.

Figure 4 Differential radial receiver functions due to S wave velocity perturbation for the case where P wave impinges under the model illustrated in Fig. 3 with incident angle of 40°. Each trace is drawn in the same amplitude scale.

Figure 5 Differential radial receiver functions due to density perturbation for the case where P wave impinges under the model illustrated in Fig. 3 with incident angle of 40°. Each trace is drawn in the same amplitude scale.

Figure 6 Differential radial receiver functions due to P wave velocity perturbation for the case where P wave impinges under the model illustrated in Fig. 3

with incident angle of 40°. Each trace is drawn in the same amplitude scale.

Figure 7 Differential radial receiver functions due to S wave velocity perturbation with P wave velocity and density adjusted by eqs. 1 and 2 for the case where P wave impinges under the model illustrated in Fig. 3 with incident angle of 40°. Each trace is drawn in the same amplitude scale.

Figure 8 True, initial and final S wave velocity models for the first experiment. We calculate synthetic P waveforms for the true model and add random noises to make pseudo-observed P waveforms. The solid line indicates the final model obtained by inverting the three pseudo-observed radial receiver functions shown by the dotted line in Fig. 9. Errors in the S wave velocity of each layer are indicated with the bars.

Figure 9 Pseudo-observed (dotted lines) and synthetic (solid lines) radial receiver functions for three incident angles. The synthetic receiver functions are calculated for the final model shown by the solid line in Fig. 8. i denotes the incident angle of P wave.

Figure 10 True, initial and final S wave velocity models for the second experiment. We calculate synthetic P waveforms for the true model and add random noises to make pseudo-observed P waveforms. The solid line indicates the final model obtained by inverting a stacked pseudo-observed radial receiver function shown by the dotted line in Fig. 11. Errors in the S wave velocity of each layer are indicated with the bars.

Figure 11 A stacked pseudo-observed (dotted lines) and a synthetic (solid lines) radial receiver function. The synthetic receiver function is calculated for the final model shown by the solid line in Fig. 10. i denotes the incident angle of P wave.

Figure 12 True, initial and final S wave velocity models for the third experiment. We calculate synthetic P waveforms for the true model and add random noises to make pseudo-observed P waveforms. The solid line indicates the final model obtained by inverting the three pseudo-observed radial receiver functions shown by the dotted line in Fig. 13. Errors in the S wave velocity of each layer are indicated with the bars.

Figure 13 Pseudo-observed (dotted lines) and synthetic (solid lines) radial receiver functions for three incident angles. The synthetic receiver functions are calculated for the final model shown by the solid line in Fig. 12. i denotes the incident angle of P wave.

Figure 14 Amplitudes of the major phases in radial receiver functions for various incident angles. The amplitude scale of the direct P phase is shown at the left side and that of the other phases is shown at the right side of the diagram.

Table 1. Location of nearby deep events

Events	Lat. N°	Lon. E°	Depth km	Distance km	Backazimuth deg	M_{JMA}	T/R	Date
T0136	36.993	134.665	396.1	168.5	13.05	5.5	0.55	Mar. 21, 1989
T0383	35.517	135.642	367.9	127.4	89.48	6.4	1.05	Apr. 12, 1990
T0346	34.502	136.443	371.2	230.5	118.53	5.5	0.85	Jan. 31, 1990
T0067	33.582	138.112	321.3	415.2	119.98	5.7	0.85	Nov. 14, 1991
T0023	33.847	137.260	363.1	333.0	122.88	5.3	0.45	Aug. 08, 1988
T0164	33.463	139.933	401.0	336.3	131.83	5.7	0.38	June 04, 1989
T0156	32.378	137.840	410.4	481.5	135.24	5.9	0.32	May 09, 1989
T0211	32.528	137.647	419.4	457.0	135.49	5.8	0.50	Aug. 03, 1989
T0009	30.270	137.785	513.6	669.5	149.31	6.8	0.24	Sep. 07, 1988
T0493	29.457	138.005	529.0	759.2	151.18	6.7	0.18	Aug. 05, 1990

M_{JMA} denotes earthquake magnitude determined by Japan Meteorological Agency.

T/R is the rms-amplitude ratio of the tangential to the radial component of a receiver function.

Date refers to Japan Standard Time.

Table 2. Location of teleseismic events

Events	Lat.	Lon.	Depth	Distance	Backazimuth	M_s	T/R	Date
	N°	E°	km	deg	deg			
T0038	-18.771	-172.415	35.0	73.95	127.73	6.8	0.92	Oct. 08, 1988
T0045	-28.644	-177.553	28.0	78.34	138.00	6.0	0.36	Oct. 11, 1988
T0138	-19.306	169.002	166.0	63.71	143.08	6.1*	0.44	Apr. 06, 1989
T0002	-5.964	148.780	53.0	43.47	158.71	6.8	0.14	July 06, 1988
T0011	-6.081	133.667	28.0	41.38	180.86	6.7	0.66	July 25, 1988

M_s denotes surface wave magnitude after PDE Monthly Listing.

* in the M_s column denotes that the value is body wave magnitude.

T/R is the rms-amplitude ratio of the tangential to the radial component of a receiver function.

Date refers to Japan Standard Time.

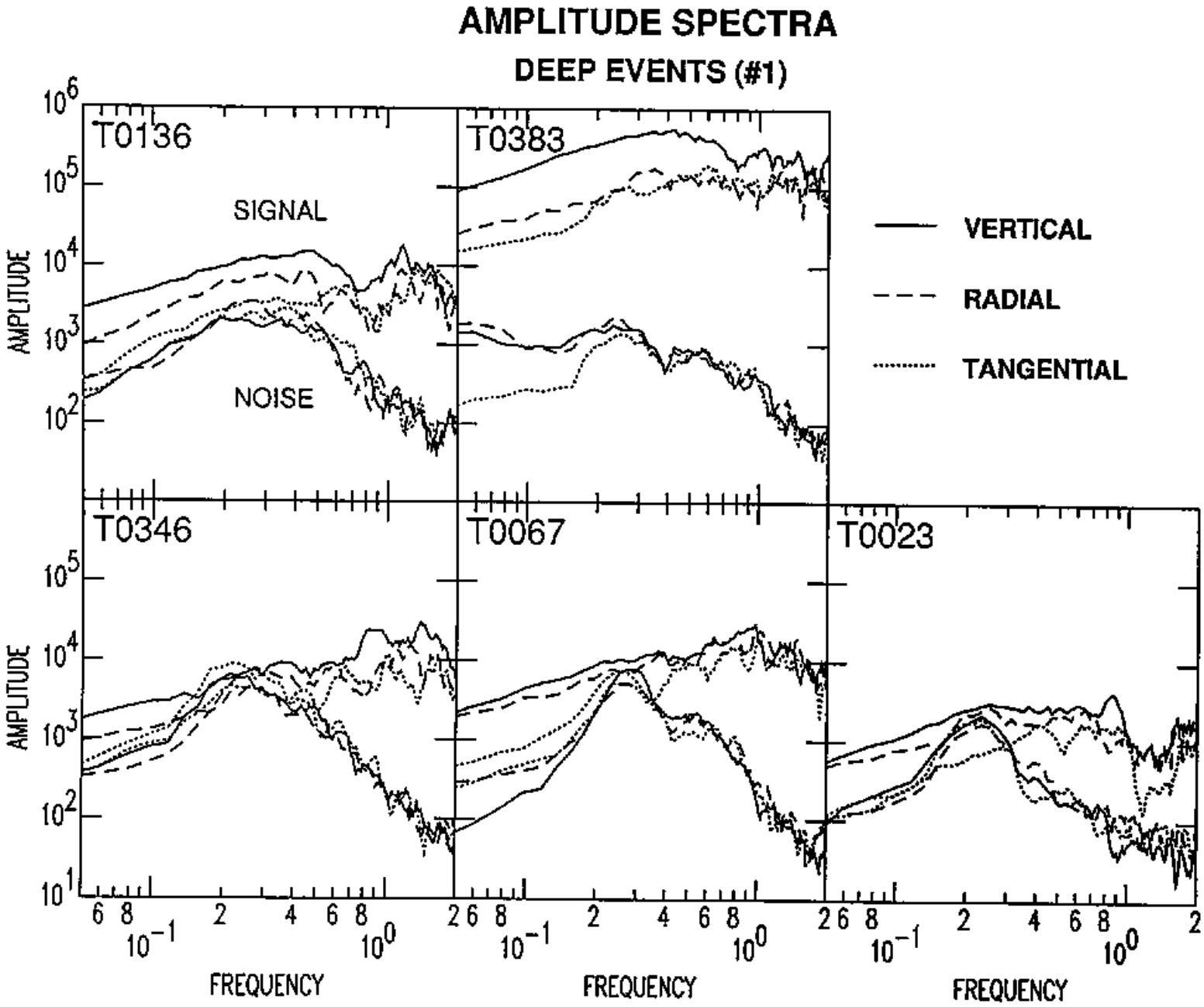
AMPLITUDE SPECTRA
DEEP EVENTS (#1)
T0136
SIGNAL
NOISE
T0383
T0346
T0067
T0023
VERTICAL
RADIAL
TANGENTIAL
AMPLITUDE
FREQUENCY

Figure 1

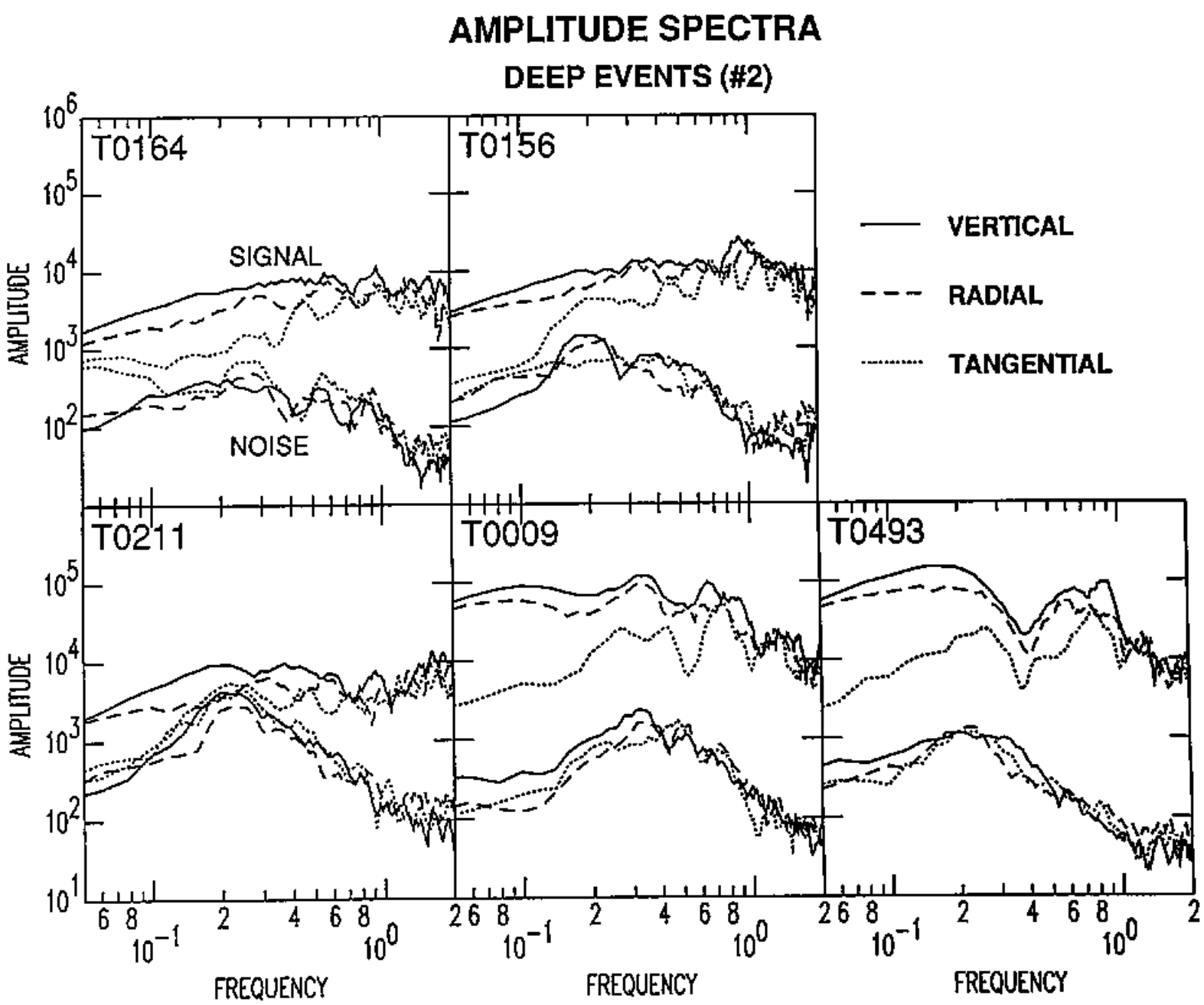
AMPLITUDE SPECTRA
DEEP EVENTS (#2)
T0164
T0156
T0211
T0009
T0493
SIGNAL
NOISE
VERTICAL
RADIAL
TANGENTIAL
AMPLITUDE
FREQUENCY

Figure 1

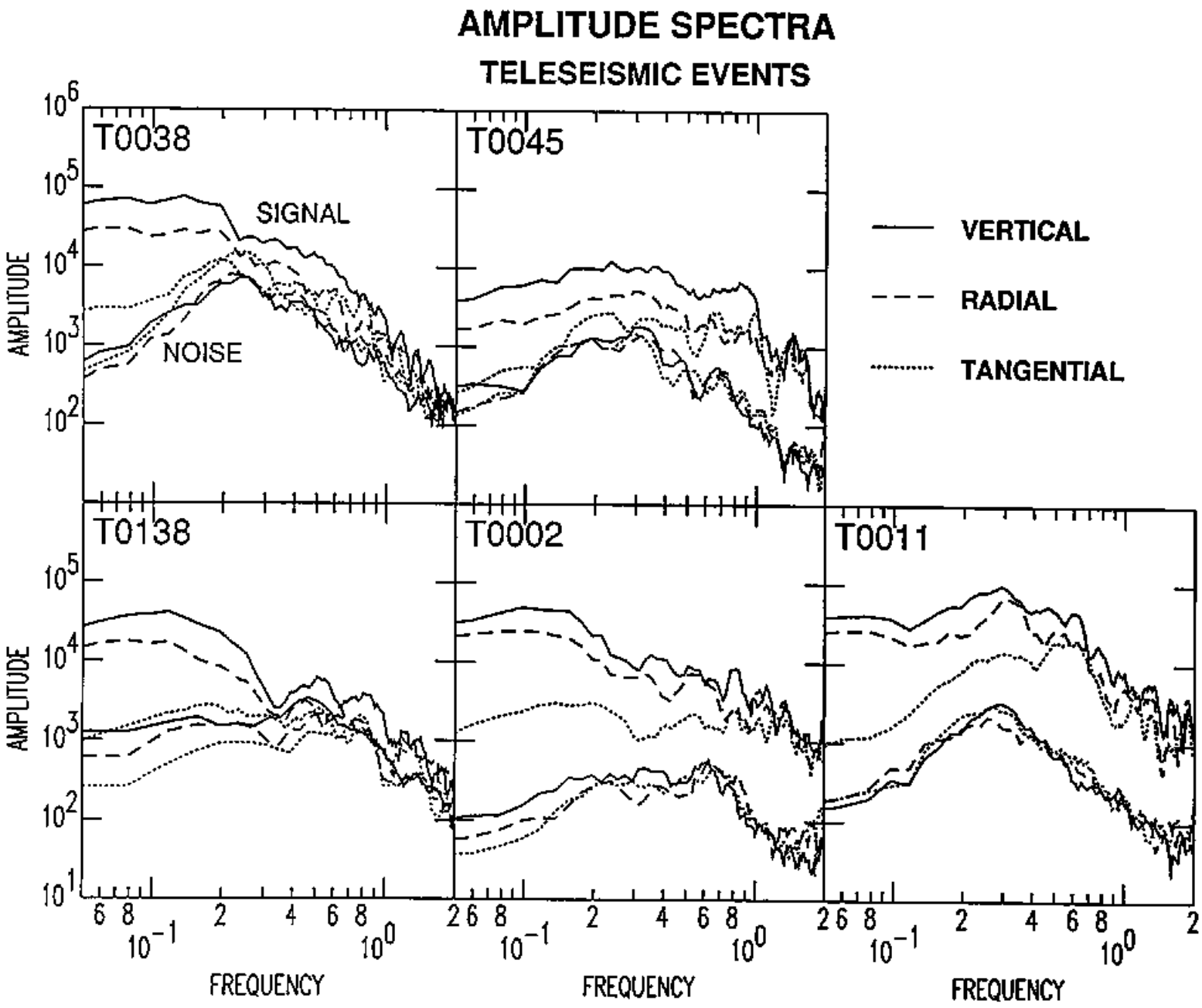
AMPLITUDE SPECTRA
TELESEISMIC EVENTS
T0038
T0045
T0138
T0002
T0011
SIGNAL
NOISE
VERTICAL
RADIAL
TANGENTIAL
AMPLITUDE
FREQUENCY

Figure 2

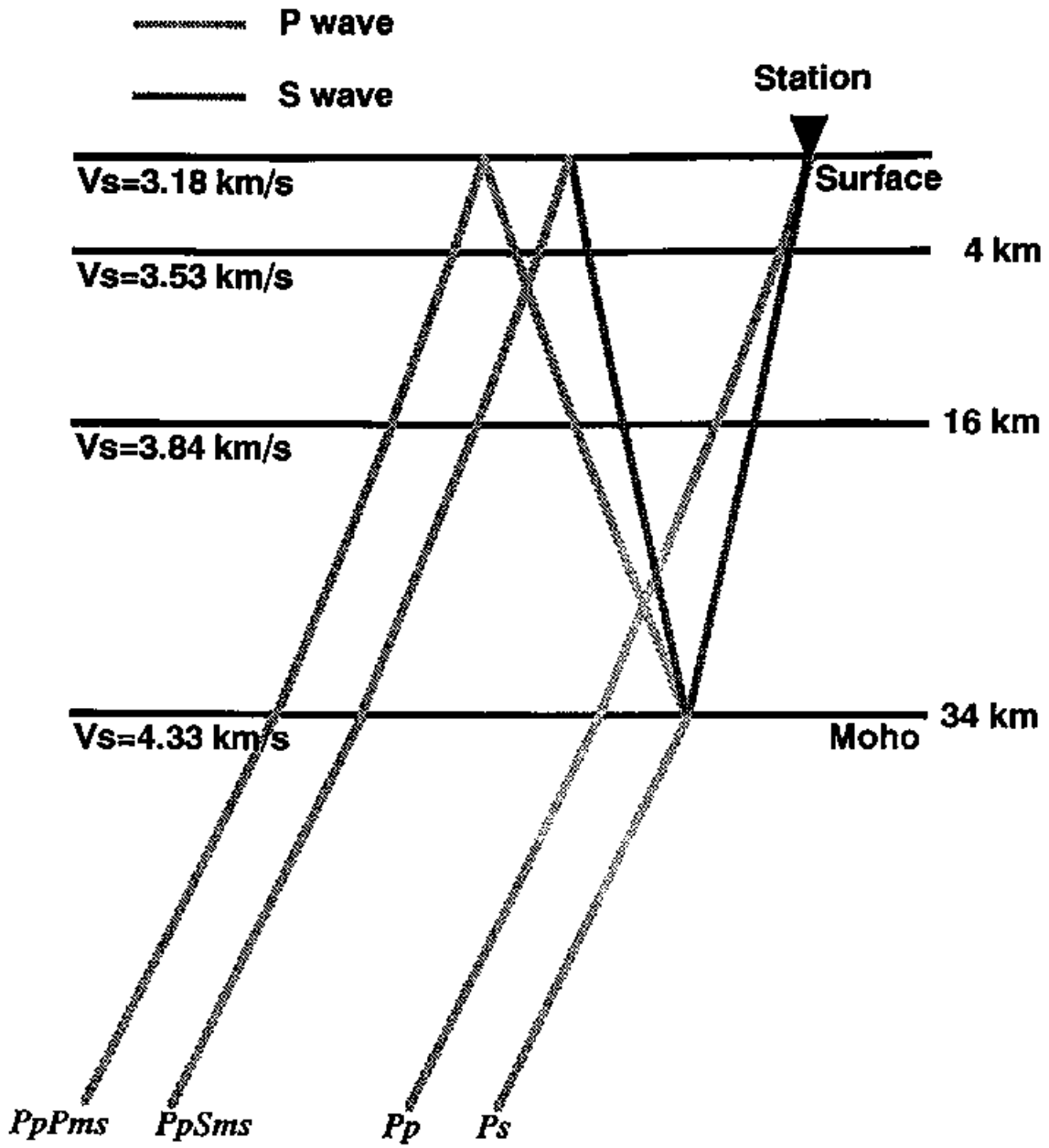
P wave
S wave
Station
Vs=3.18 km/s
Surface
4 km
Vs=3.53 km/s
16 km
Vs=3.84 km/s
34 km
Vs=4.33 km/s
Moho
PpPms
PpSms
Pp
Ps

Figure 3

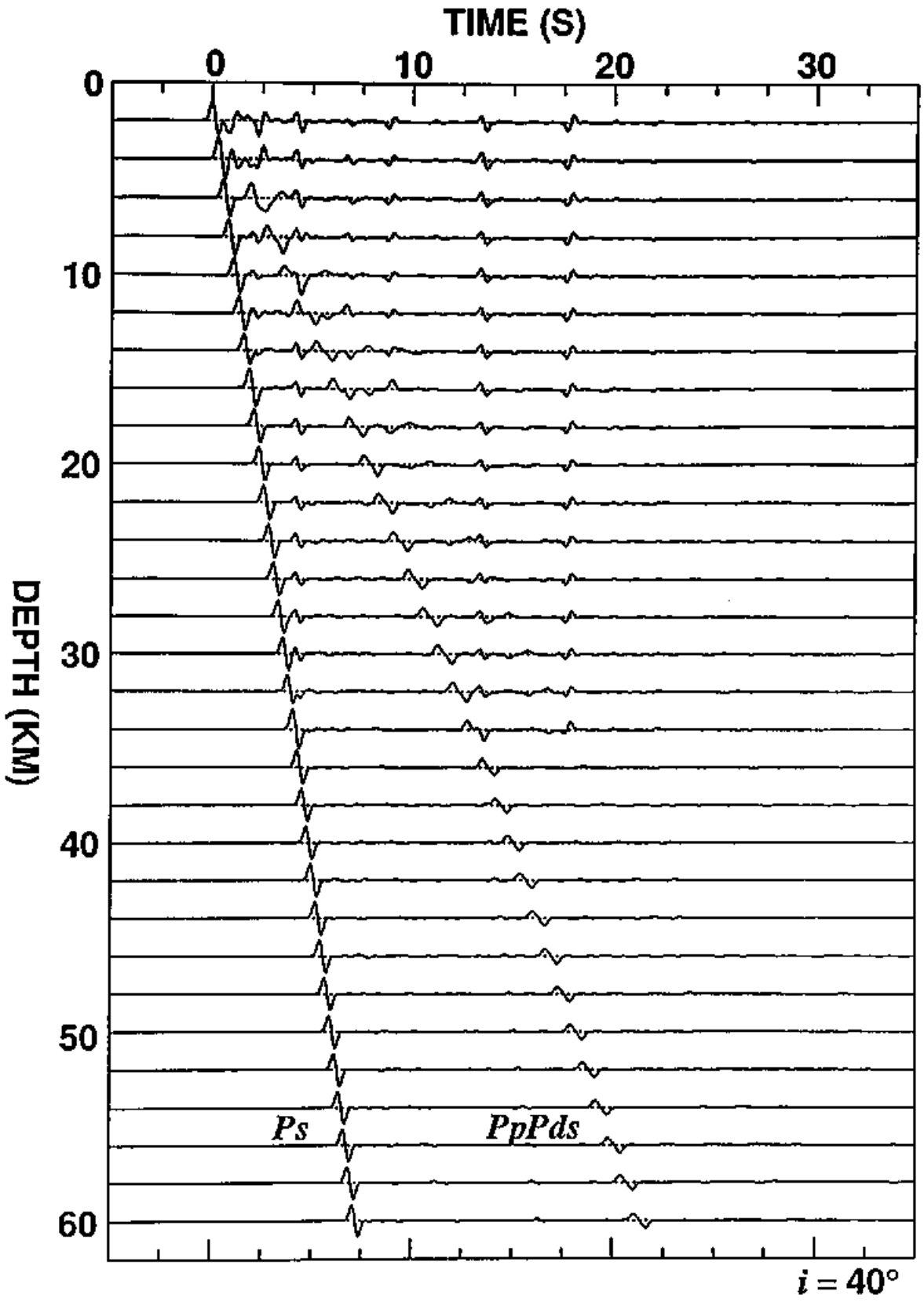
DIFFERENTIAL RADIAL RECEIVER FUNCTIONS
(S-VELOCITY PERTURBATION)
TIME (S)
0
10
20
30
DEPTH (KM)
0
10
20
30
40
50
60
Ps
PpPds
i = 40°

Figure 4

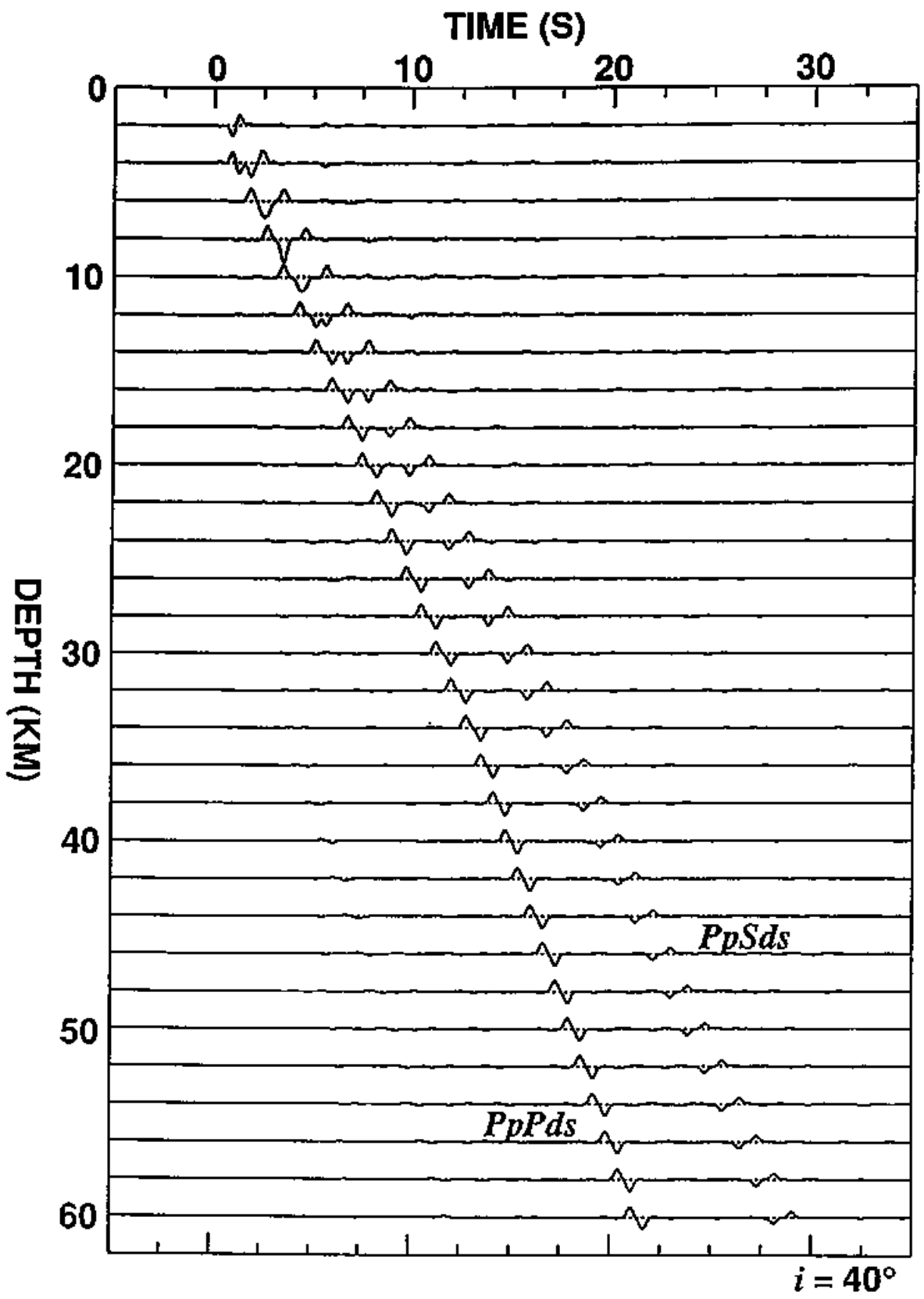
DIFFERENTIAL RADIAL RECEIVER FUNCTIONS
(DENSITY PERTURBATION)
TIME (S)
0
10
20
30
DEPTH (KM)
0
10
20
30
40
50
60
PpSds
PpPds
i = 40°

Figure 5

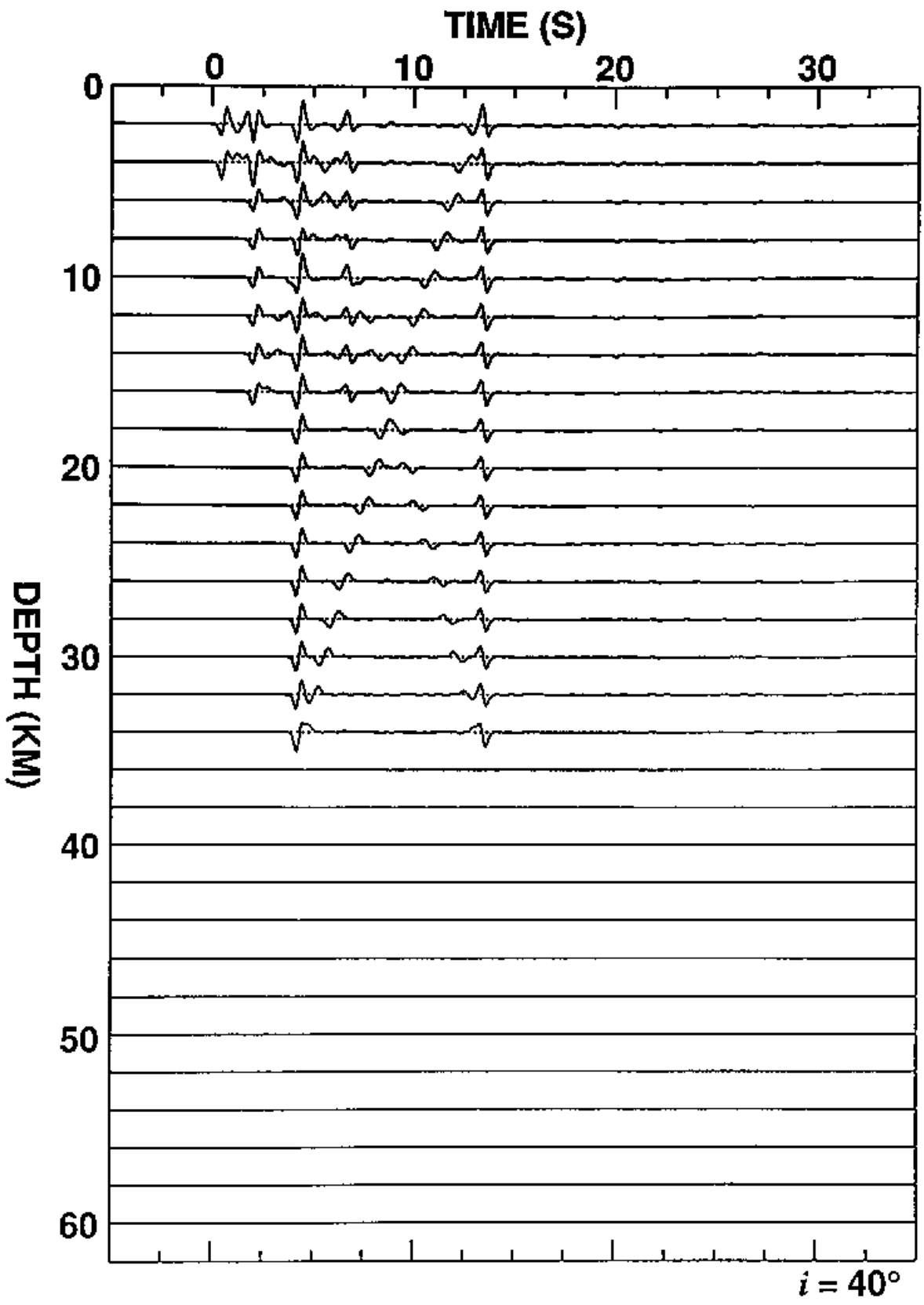
DIFFERENTIAL RADIAL RECEIVER FUNCTIONS
(P-VELOCITY PERTURBATION)
TIME (S)
0
10
20
30
DEPTH (KM)
0
10
20
30
40
50
60
i = 40°

Figure 6

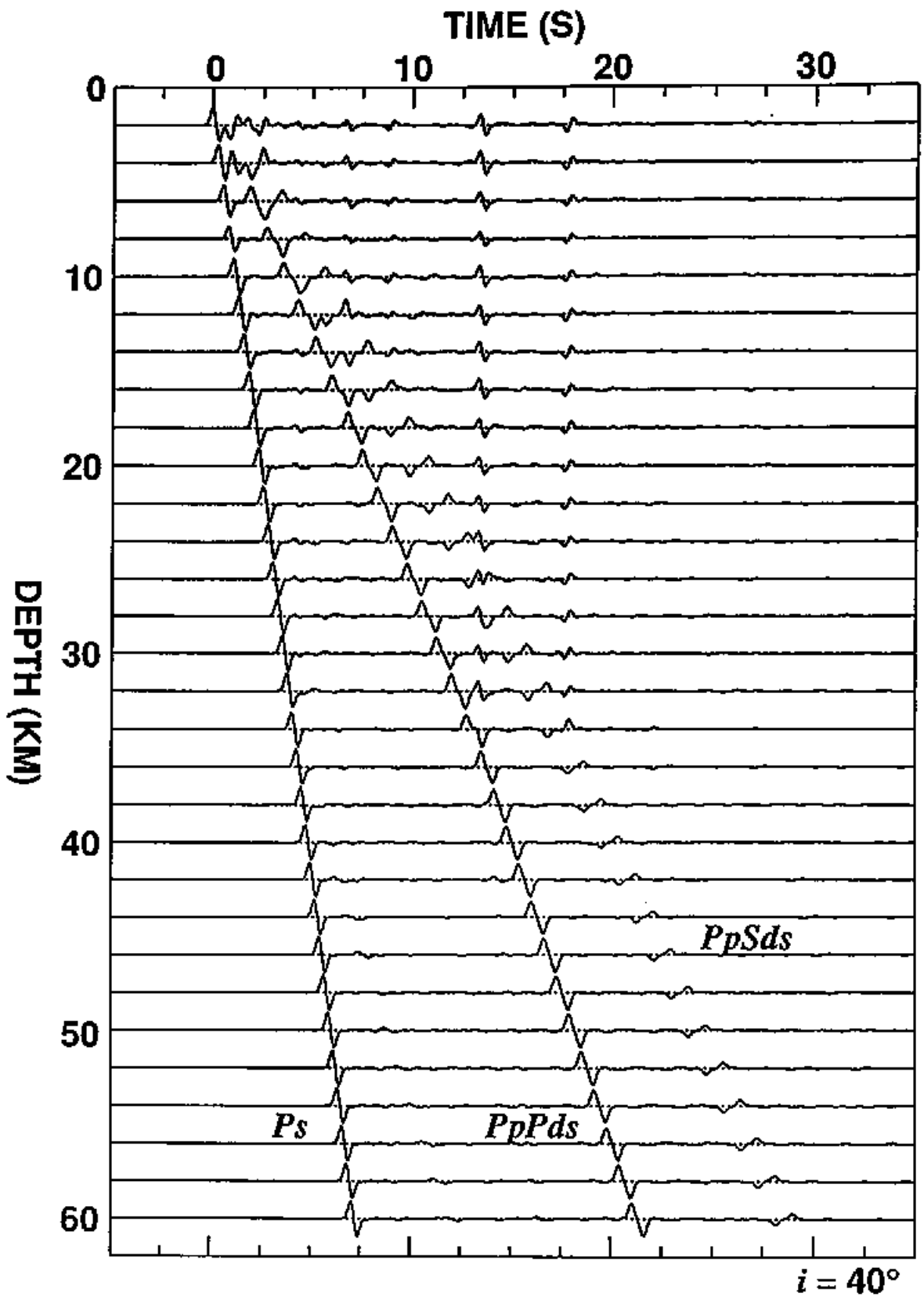
DIFFERENTIAL RADIAL RECEIVER FUNCTIONS
(FULL PERTURBATION)
TIME (S)
0
10
20
30
DEPTH (KM)
0
10
20
30
40
50
60
PpSds
Ps
PpPds
i = 40°

Figure 7

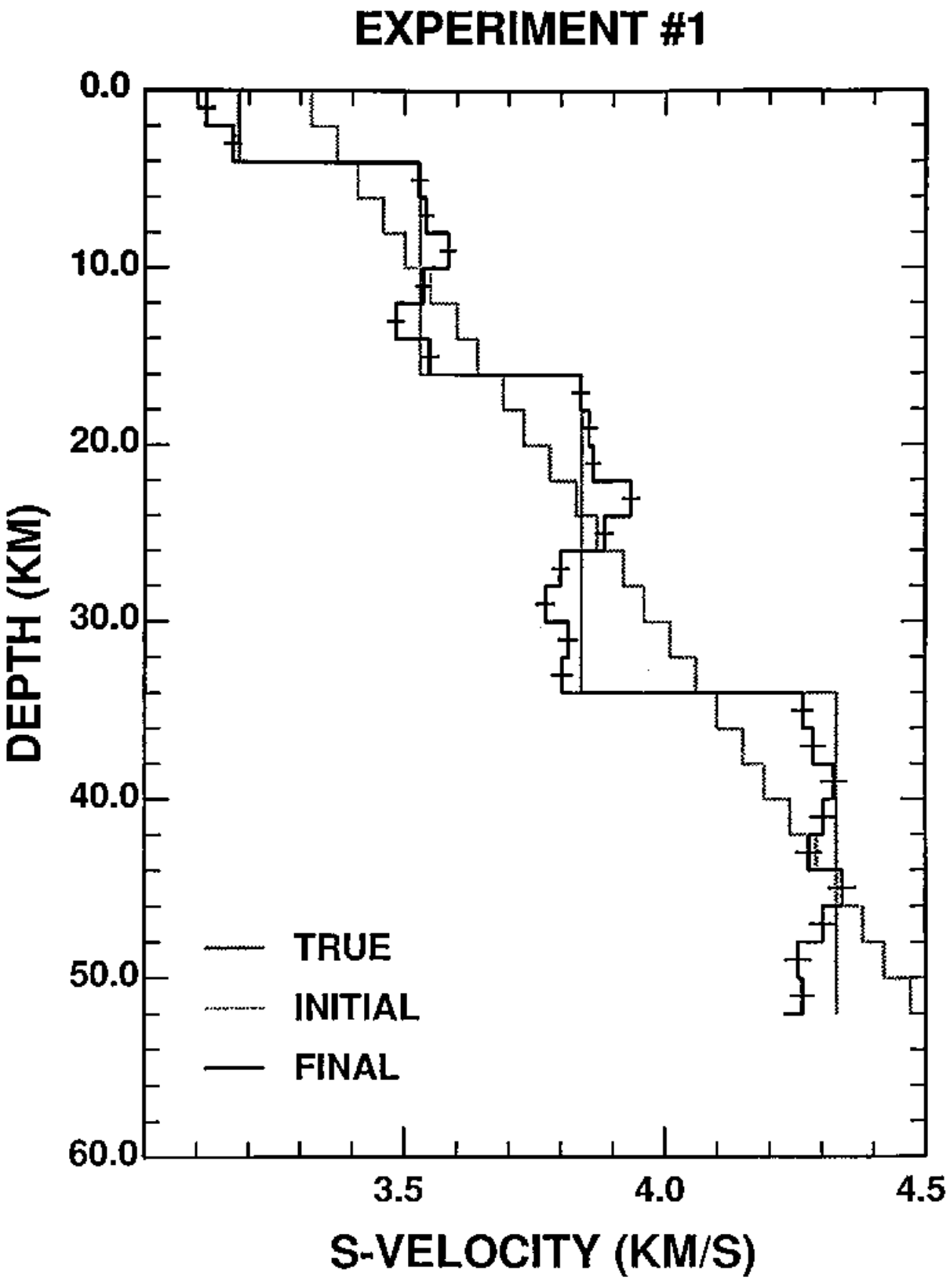
EXPERIMENT #1
0.0
10.0
20.0
30.0
40.0
50.0
60.0
DEPTH (KM)
TRUE
INITIAL
FINAL
3.5
4.0
4.5
S-VELOCITY (KM/S)

Figure 8

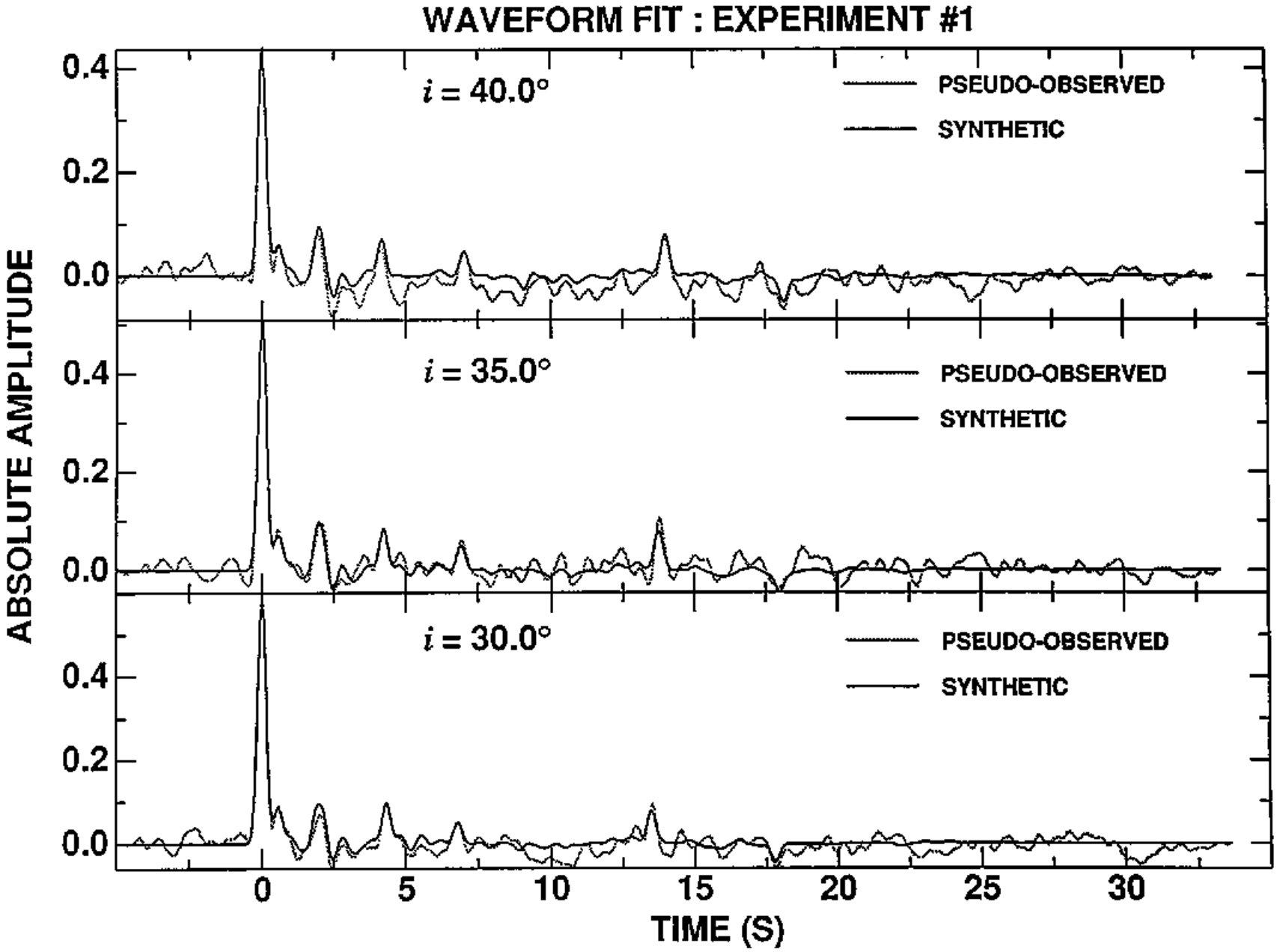
WAVEFORM FIT : EXPERIMENT #1
ABSOLUTE AMPLITUDE
0.4
0.2
0.0
i = 40.0°
PSEUDO-OBSERVED
SYNTHETIC
i = 35.0°
PSEUDO-OBSERVED
SYNTHETIC
i = 30.0°
PSEUDO-OBSERVED
SYNTHETIC
0
5
10
15
20
25
30
TIME (S)

Figure 9

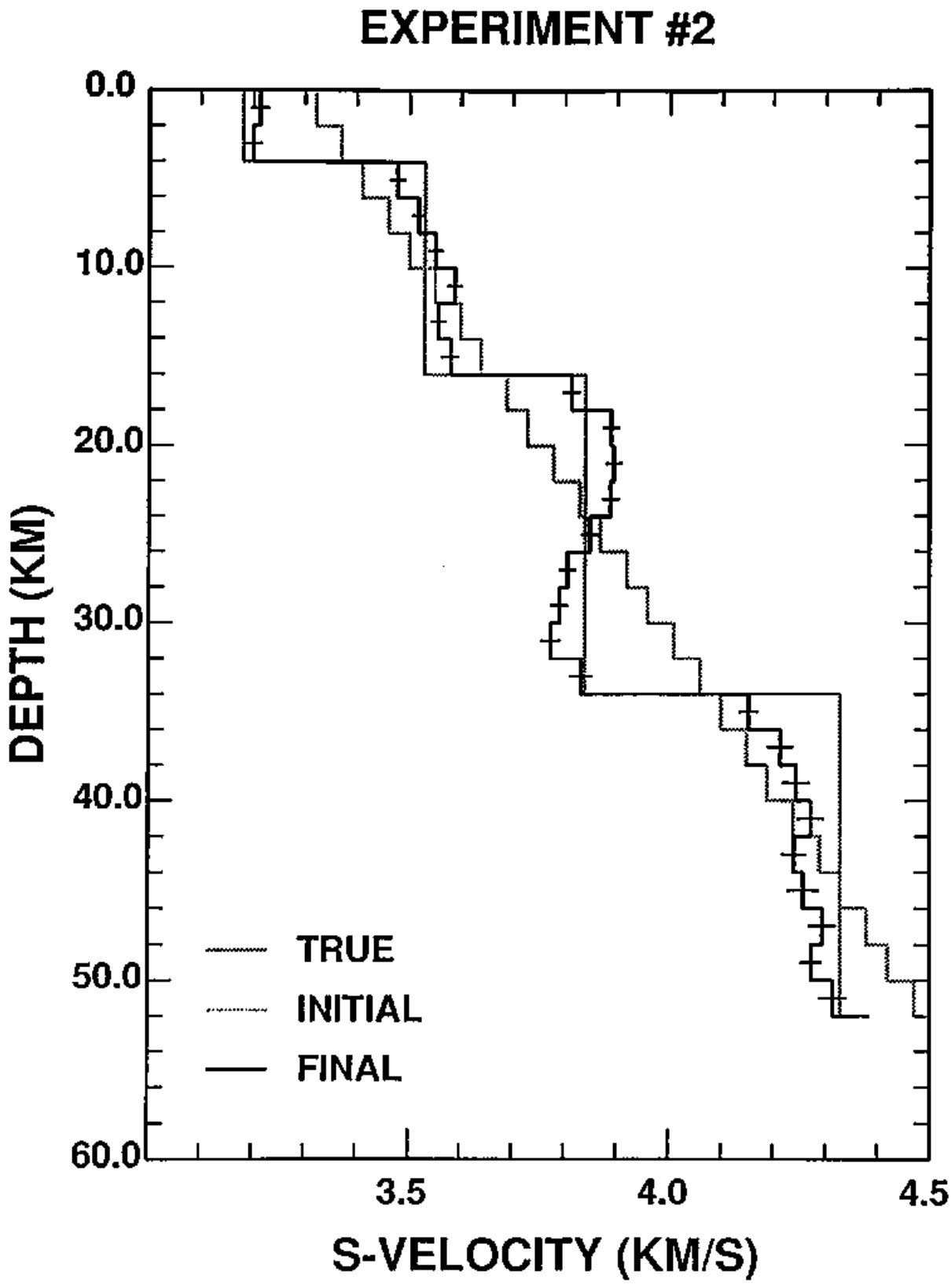
EXPERIMENT #2
0.0
10.0
20.0
30.0
40.0
50.0
60.0
DEPTH (KM)
TRUE
INITIAL
FINAL
3.5
4.0
4.5
S-VELOCITY (KM/S)

Figure 10

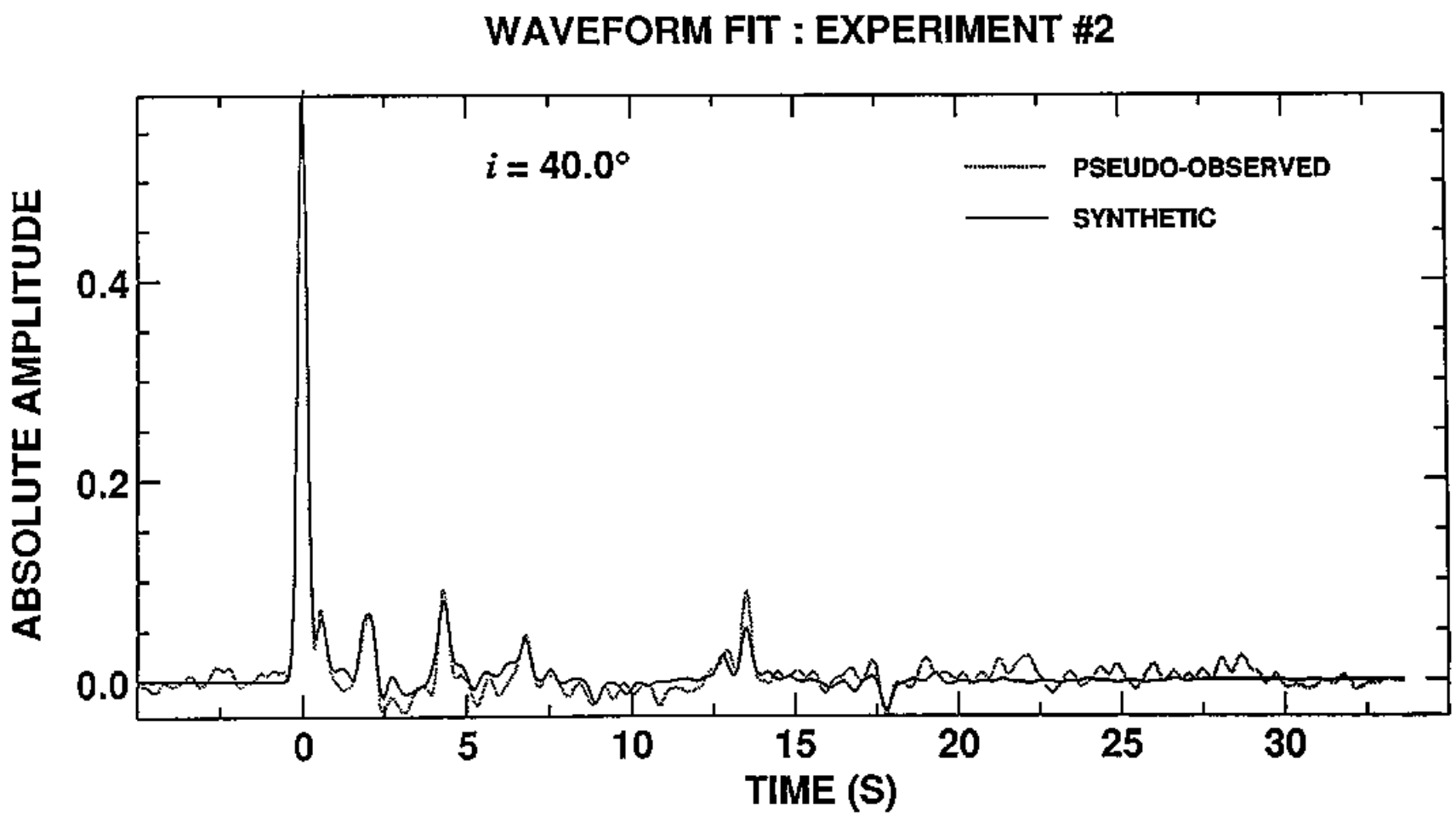
WAVEFORM FIT : EXPERIMENT #2
i = 40.0°
PSEUDO-OBSERVED
SYNTHETIC
ABSOLUTE AMPLITUDE
0.0
0.2
0.4
0
5
10
15
20
25
30
TIME (S)

Figure 11

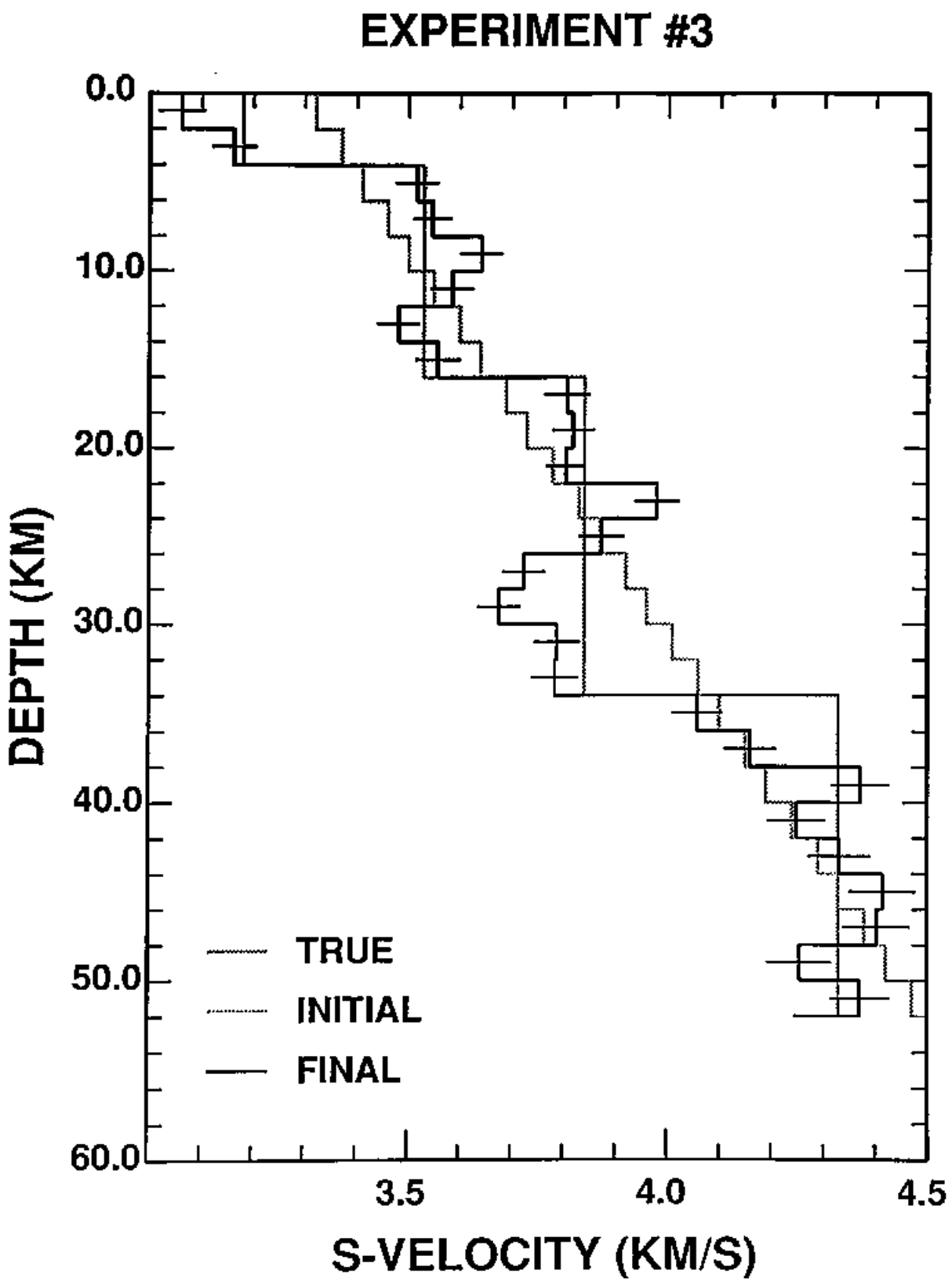
EXPERIMENT #3
0.0
10.0
20.0
30.0
40.0
50.0
60.0
DEPTH (KM)
TRUE
INITIAL
FINAL
3.5
4.0
4.5
S-VELOCITY (KM/S)

Figure 12

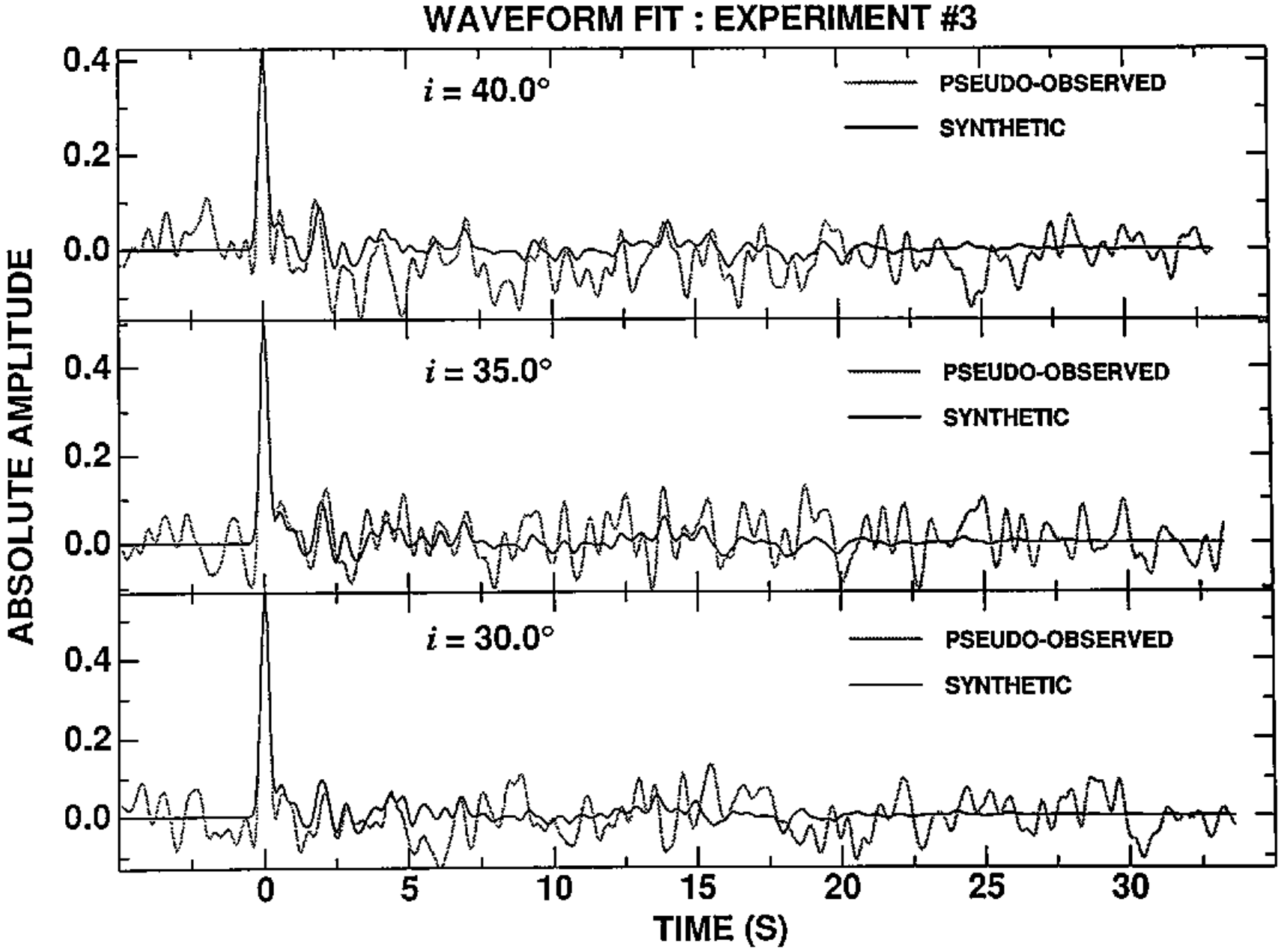
WAVEFORM FIT : EXPERIMENT #3
ABSOLUTE AMPLITUDE
0.4
0.2
0.0
i = 40.0°
PSEUDO-OBSERVED
SYNTHETIC
i = 35.0°
PSEUDO-OBSERVED
SYNTHETIC
i = 30.0°
PSEUDO-OBSERVED
SYNTHETIC
0
5
10
15
20
25
30
TIME (S)

Figure 13

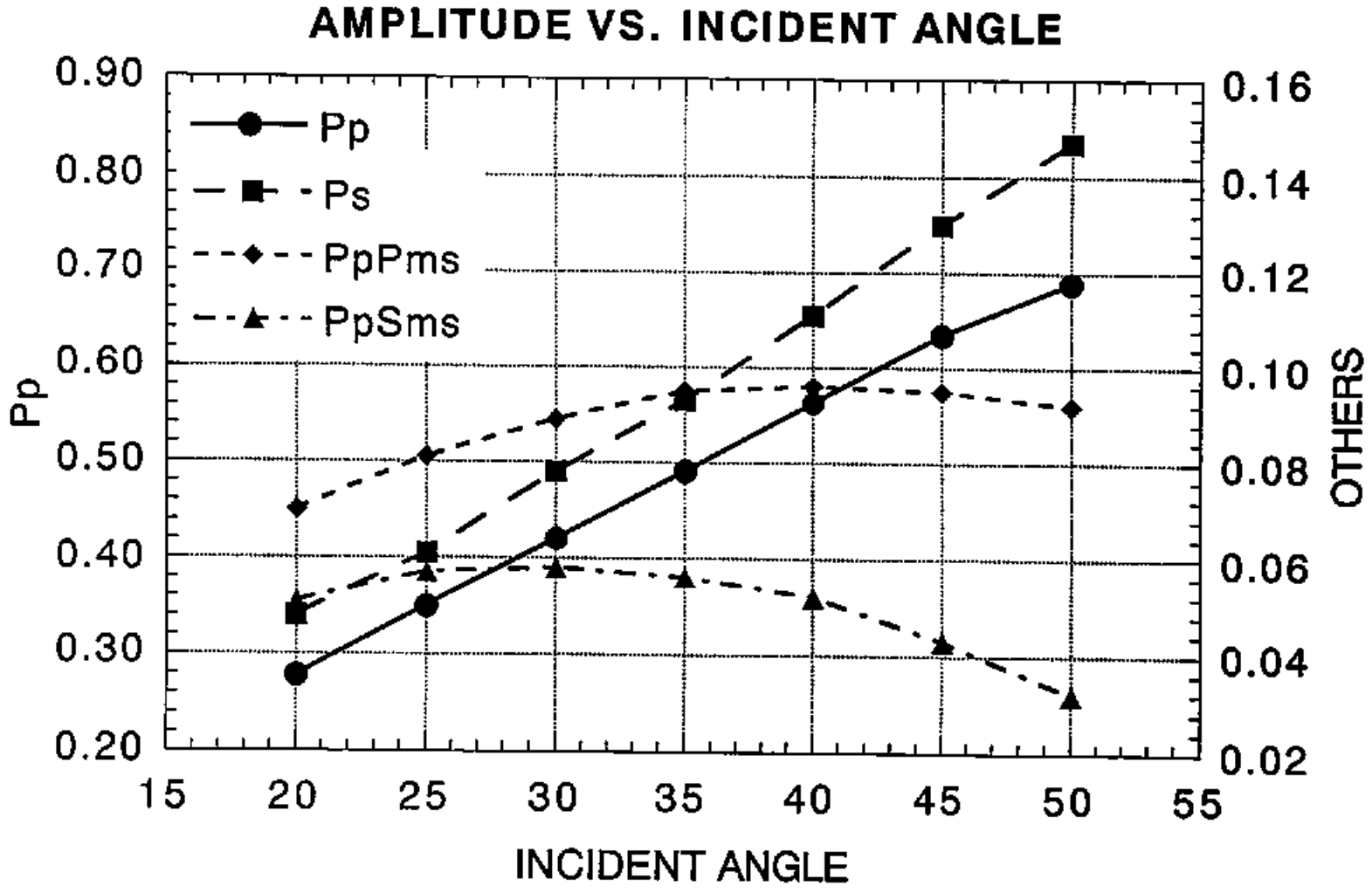
AMPLITUDE VS. INCIDENT ANGLE
Pp
Ps
PpPms
PpSms
0.90
0.80
0.70
0.60
0.50
0.40
0.30
0.20
0.16
0.14
0.12
0.10
0.08
0.06
0.04
0.02
15
20
25
30
35
40
45
50
55
INCIDENT ANGLE
OTHERS

Figure 14